Check for updates

JGR Solid Earth

RESEARCH ARTICLE
10.1029/2019JB019100

Wide-Angle Seismic Imaging of Two Modes of Crustal Accretion in Mature Atlantic Ocean Crust

R. G. Davy[1], J. S. Collier[1], T. J. Henstock[2], and The VoiLA Consortium

[1]Department of Earth Sciences and Engineering, Imperial College London, London, UK, [2]Ocean and Earth Science, National Oceanography Centre Southampton, University of Southampton, Southampton, UK

Key Points:
- We identify that magmatic and tectonic modes of slow Atlantic crustal accretion are distinct and equal, based on seismic characteristics
- The structure of crustal discontinuities is controlled by the accretion mode of neighboring segments, independent of ridge offset and order
- Two buried oceanic core complexes in mature Atlantic Ocean crust are identified, based on their dimensions and seismic structure

Supporting Information:
- Supporting Information S1

Correspondence to:
R. G. Davy,
r.davy@imperial.ac.uk

Citation:
Davy, R. G., Collier, J. S., Henstock, T. J., & The VoiLA Consortium (2020). Wide-angle seismic imaging of two modes of crustal accretion in mature Atlantic Ocean crust. *Journal of Geophysical Research: Solid Earth*, *125*, e2019JB019100. https://doi.org/10.1029/2019JB019100

Received 25 NOV 2019
Accepted 16 APR 2020
Accepted article online 28 APR 2020

© 2020. The Authors.
This is an open access article under the terms of the Creative Commons Attribution License, which permits use, distribution and reproduction in any medium, provided the original work is properly cited.

Abstract We present a high-resolution 2-D P-wave velocity model from a 225-km-long active seismic profile, collected over ~60–75 Ma central Atlantic crust. The profile crosses five ridge segments separated by a transform and three nontransform offsets. All ridge discontinuities share similar primary characteristics, independent of the offset. We identify two types of crustal segment. The first displays a classic two-layer velocity structure with a high gradient Layer 2 (~0.9 s^{-1}) above a lower gradient Layer 3 (0.2 s^{-1}). Here, PmP coincides with the 7.5 km s^{-1} contour, and velocity increases to >7.8 km s^{-1} within 1 km below. We interpret these segments as magmatically robust, with PmP representing a petrological boundary between crust and mantle. The second has a reduced contrast in velocity gradient between the upper and lower crust and PmP shallower than the 7.5 km s^{-1} contour. We interpret these segments as tectonically dominated, with PmP representing a serpentinized (alteration) front. While velocity-depth profiles fit within previous envelopes for slow-spreading crust, our results suggest that such generalizations give a misleading impression of uniformity. We estimate that the two crustal styles are present in equal proportions on the floor of the Atlantic. Within two tectonically dominated segments, we make the first wide-angle seismic identifications of buried oceanic core complexes in mature (>20 Ma) Atlantic Ocean crust. They have a ~20-km-wide "domal" morphology with shallow basement and increased upper crustal velocities. We interpret their midcrustal seismic velocity inversions as alteration and rock-type assemblage contrasts across crustal-scale detachment faults.

1. Introduction

Oceanic crust is the site of major heat and mass flux exchange between the solid Earth and the oceans and atmosphere. From its creation at mid-ocean ridges to its consumption at subduction zones, it is a buffer of elements such as carbon and volatiles such as water. Early active-source seismic experiments showed a distinct two-layer structure, which was inferred to hold true for most oceanic settings (e.g., White et al., 1992). The upper igneous crust (Layer 2) is typically 1–2 km thick and is identified by a high P-wave velocity gradient (~1.0 s^{-1}), while the lower crust (Layer 3) is 4–6 km thick and has a higher-velocity (>6.4 km s^{-1}) but significantly lower-velocity gradient (~0.1 s^{-1}). In young crust, rapid increases in Layer 2 velocities were attributed to crack closure by precipitation of hydrothermal alteration products (Grevemeyer & Weigel, 1997; Houtz & Ewing, 1976). By comparison with ophiolites, the seismic structure was interpreted as an upper crust of extrusive basaltic flows and dolerite dikes, overlying a gabbroic lower crust (commonly referred to as the "Penrose model," Anonymous, 1972). An issue that remains much debated is the interpretation of the PmP reflection and whether this represents the base of the petrological crust or a serpentinization front due to infiltration of water and alteration of olivine (e.g., Minshull et al., 1998). The classic White et al. (1992) velocity-depth envelopes have been updated recently by Grevemeyer et al. (2018) and Christeson et al. (2019), who exclude some of the older surveys with inherent resolution issues and include recent surveys that used more modern instrumentation and techniques. While some modifications were made, the broad concept of a unified 1-D velocity structure of oceanic crust was upheld.

Nevertheless, it has been known for some time that processes at mid-ocean ridges vary along axis, and it has been suggested that ridge segmentation results in a hierarchical pattern of melt delivery from the mantle (Langmuir et al., 1986; Macdonald et al., 1988). Significant crustal thinning toward first- (transform fault) and possibly second-order (nontransform offsets [NTOs] at slow-spreading ridges) discontinuities was suggested by Detrick et al. (1993). At these discontinuities, the oceanic crust thins laterally over tens of kilometers, accommodated primarily in Layer 3, which may even be absent beneath the discontinuity itself.

The thinning was shown to have little dependence on the size of ridge axis offset, although a majority of the studies targeted a single discontinuity that hampers the comparison of results. More recently, Carbotte et al. (2016) revisited the observations made at ridge axes and also concluded that both first- and second-order ridge discontinuities, irrespective of offset, provide major physical boundaries in ridge properties and, hence, melt supply.

The advent of high-resolution bathymetric mapping has shown that large sections of the slow-spreading Mid-Atlantic Ridge (MAR) are characterized by large detachment faults that expose oceanic core complexes (OCCs) (Cann et al., 1997; Cannat et al., 1997; Smith et al., 2006; Tucholke et al., 1998). As a result of this unexpected discovery, the majority of recent seismic studies in the Atlantic have explored the ridge axis to investigate the implications for crustal accretion (Figure 1). This work led to the development of a new concept that slow-spreading oceanic crust is formed by two modes of accretion: magmatically robust and tectonically controlled (Escartin et al., 2008). Magmatic crust is described by the Penrose model, formed through melt delivery at the center of the segment and is symmetric about the spreading ridge (e.g., experiments labeled 17–20, 23, and 28 in Figure 1) (e.g., Hooft et al., 2000; Hosford et al., 2001; Lin & Phipps Morgan, 1992; Tolstoy et al., 1993). Conversely, tectonically controlled accretion occurs where melt supply is limited, and much of the extension is accommodated along long-lived detachment faults, leading to asymmetric crustal accretion (e.g., 6, 9–10, 12, 14, 16, 21–22, and 28 in Figure 1) (Dick et al., 2008; Escartin et al., 2008). This mode of crustal accretion is commonly referred to as the "Chapman model" (Escartín & Canales, 2011). Exhumation of lower crustal and/or upper mantle rocks along the detachment faults form blocky, dome-shaped OCCs, commonly found at segment ends (Dannowski et al., 2010; Smith et al., 2003). Seismic refraction studies of OCCs at the MAR, such as the Kane OCC, Atlantis Massif, and the Trans-Atlantic Geotraverse (TAG) hydrothermal mound (e.g., 12, 14, and 16 in Figure 1), reveal highly heterogeneous seismic velocity structures (Canales et al., 2007; Canales et al., 2008; Collins et al., 2009; Dunn et al., 2017; Harding et al., 2017). These variations are attributed to diverse assemblages of gabbroic plutons and ultramafic rocks, coupled with variations in hydration and serpentinization of olivine-rich rocks, and fracturing of the OCC footwall (Canales et al., 2008; Escartín et al., 2003; Ildefonse et al., 2007; MacLeod et al., 2002; MacLeod et al., 2009). However, petrological/alteration interpretations of seismic structures are nonunique, and studies have relied on seafloor sampling and drilling for ground truthing (Blackman et al., 2014; Blackman et al., 2019; Canales et al., 2008; Collins et al., 2009). Given these reported heterogeneities, it is important to assess the applicability of a generalized 1-D velocity envelope for slow-spreading crust.

While there have been many new insights at the ridge axis, most of these seismic studies span a limited number of segments and are often impeded by extreme seafloor topography. The single published account of an off-axis Atlantic seismic study conducted since 2000 (4 in Figure 1, Lizarralde et al. (2004)) used very long offsets to target mantle structure along a flow line between 108 and 157 Ma. Our study, presented here, investigates the seismic structure across five crustal segments, bound by first- and second-order discontinuities, of 60–75 Ma Atlantic crust and obtains a velocity model with a resolution of just 5.0 by 2.5 km, or better. We test the traditional models of vertical and lateral velocity structure, hierarchical segmentation and gain new insights into the generation of slow-spreading oceanic lithosphere.

2. Tectonic Setting

The study area lies in the western central Atlantic and formed as part of the North American plate between 60 and 75 Ma with a spreading half rate of around 23 mm yr^{-1} (Figure 1, Klitgord & Schouten, 1986; Müller & Roest, 1992; Müller & Smith, 1993; Müller et al., 1999). The seismic profile presented here is 225 km long and oriented parallel to the MAR. It extends from ~25 km south of the Barracuda Ridge (~15.7°N, 55.3°W) southward across the Demerara Abyssal Plain (Figure 2a). To assess the seafloor spreading fabric in the region, we used potential field data (satellite altimetry-derived gravity, Sandwell et al., 2014, Figure 2a; shipboard magnetics, Allen et al., 2019, Figure 2b). There is some uncertainty in the interpretation of the magnetic anomalies due to the data quality (the grid includes data dating from the 1960s) and due to the region's low latitude. Therefore, to constrain the interpretation further, we used fracture zone (FZ) traces automatically extracted from the satellite gravity by Wessel et al. (2015). We needed to manually extend some of these traces westward to intersect our seismic line. To help differentiate between first-order (transform fault) and second-order (NTO) traces and identify magnetic anomalies, we computed synthetic flow lines within the

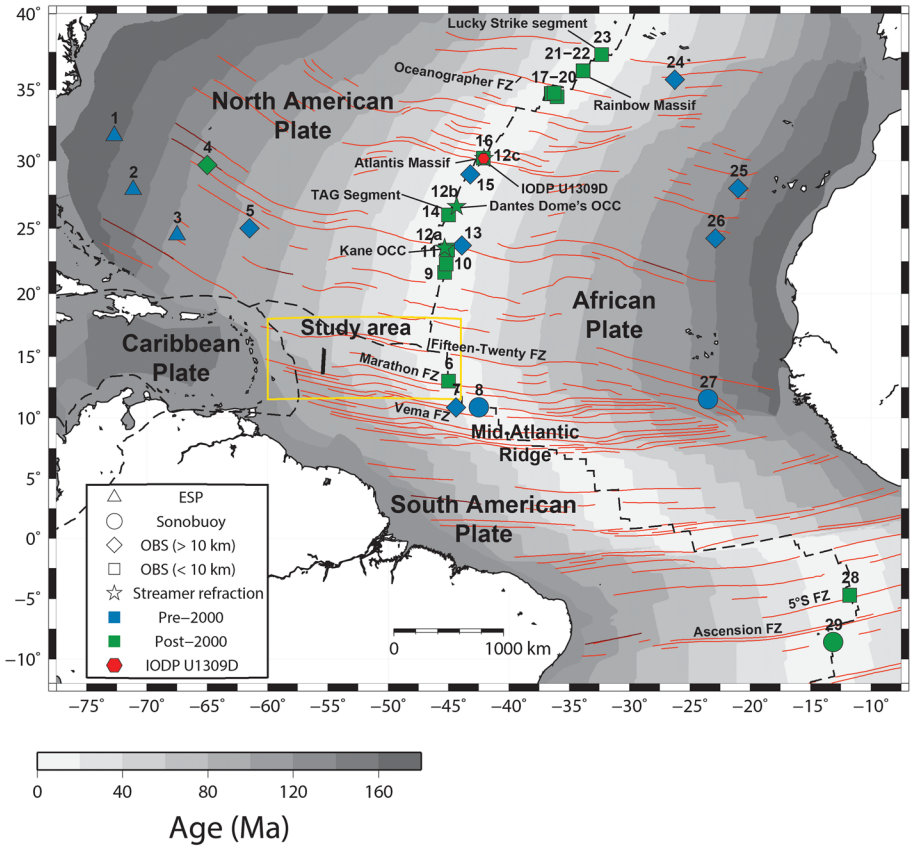

Figure 1. Seafloor age of the central and equatorial Atlantic (Müller et al., 2019). Red lines are fracture zones automatically picked from satellite altimetry by Wessel et al. (2015). Black dashed lines are plate boundaries according to Bird (2003). The bold line marks the seismic profile presented here with the yellow box the area shown in Figure 2a. Red hexagon indicates the location of IODP Hole U1309D (Blackman et al., 2006). Numbered symbols mark previous seismic experiments. We subdivide these into those published before and after 2000 in recognition of the discovery of crustal-scale detachment faulting in 1997 (Cann et al., 1997) and the advent of high-resolution refraction experiments (1: Mithal & Mutter, 1989; 2 Minshull et al., 1991; 3: NAT Study Group, 1985; 4: Lizarralde et al., 2004; 5: Whitmarsh et al., 1983; 6: Peirce et al., 2019; 7: Potts et al., 1986; 8: Ludwig & Rabinowitz, 1980; 9: Dannowski et al., 2018; 11: Canales et al., 2000; 12: Canales et al., 2008; 13: Abrams et al., 1988; 14: (Canales et al., 2007); 15: Wolfe et al., 1995; 16: Collins et al., 2009; 17: Dunn et al., 2005; 18: Hooft et al., 2000; 19: Canales, Detrick, et al., 2000; 20: Hosford et al., 2001; 21: Canales et al., 2017; 22: Dunn et al., 2017; 23: Seher et al., 2010; 24: Potts et al., 1986; 25: Collier et al., 1998; 26: Henstock et al., 1996; 27: Spathopoulos & Jones, 1993; 28: Planert et al., 2009; and 29: Minshull et al., 2003).

GPlates software using combinations of North-West African and North/South American rotation poles from Müller et al. (2019) after Harmon et al. (2019) (colored circles in Figure 2a).

Our seismic line crosses the Marathon FZ and terminates close to the Mercurius FZ, both of which are first-order discontinuities and are clearly seen in the potential field data (Figures 2a and 2b). In addition, two NTOs are seen in the gravity and magnetic data and a third NTO in the magnetic data alone. The three second-order discontinuities, which we refer to as NTO-1, NTO-2, and NTO-3, displace the magnetic anomalies in a right-lateral sense by 10–30 km (0.4–1.3 Ma age difference). In contrast, the Marathon and Mercurius FZs both displace the magnetic anomalies in a left-lateral sense by 60 and 30 km, respectively (2.6 and 1.3 Ma age difference, respectively). The identified discontinuities bound five regions, which we refer to as Segments 1–5, from north to south, respectively (Figure 2c).

3. Data

3.1. Data Acquisition and Processing

This study uses wide-angle refraction and multichannel reflection seismic data collected by the RSS James Cook in May–June 2017 (Collier, 2017). The wide-angle refraction experiment used 54 OBS (four-

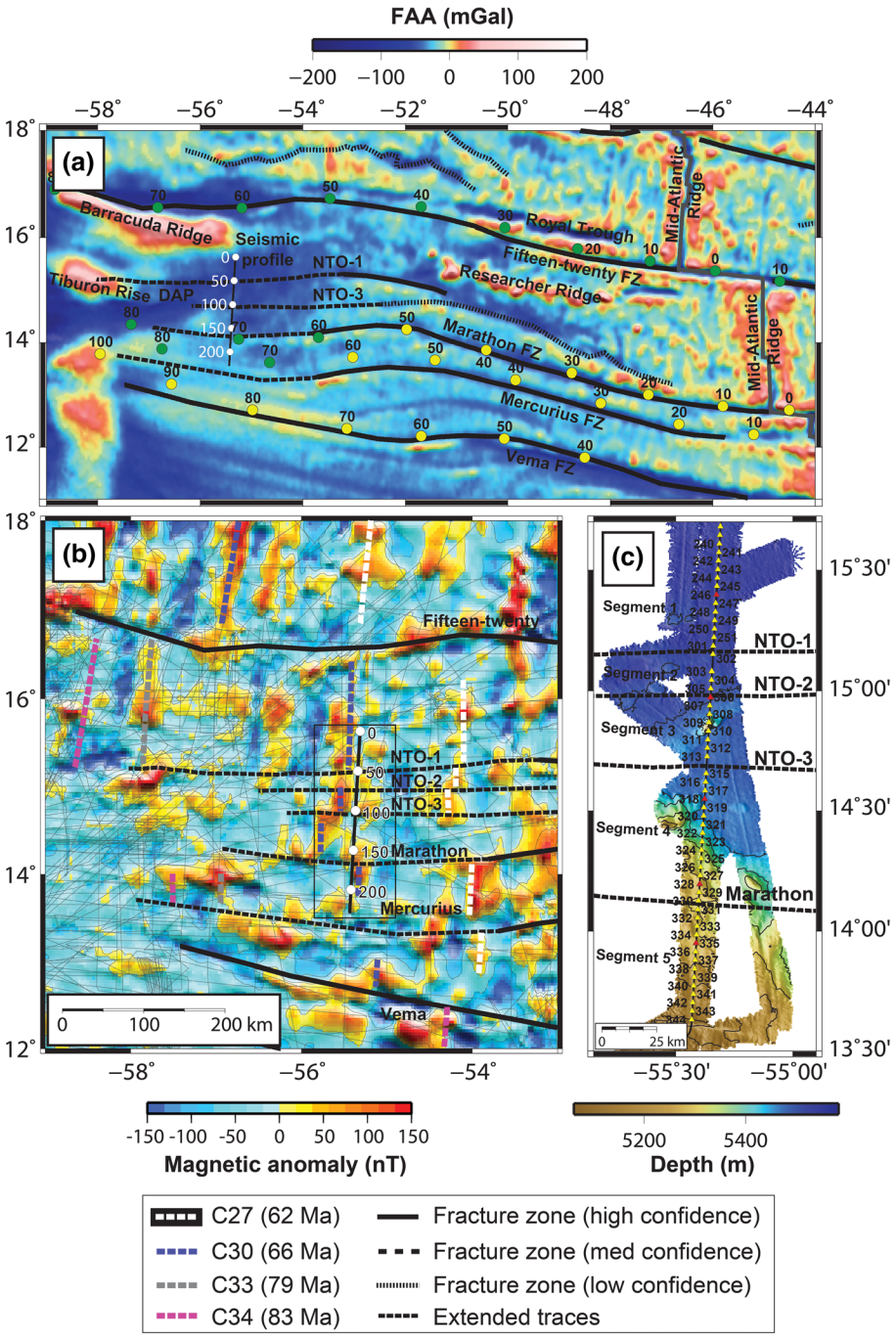

Figure 2. Seafloor spreading fabric from potential field data: (a) satellite altimetry-derived free-air gravity (Sandwell et al., 2014). Black lines are fracture zones and nontransform discontinuities (NTOs) automatically picked through gravity minima at three levels of confidence by Wessel et al. (2015). The three NTOs in our study area have been manually traced westward to intersect the seismic model line. Large circles are ages in Ma along synthetic fracture zone flow lines calculated in GPlates (measured from the center of the associated transform fault) (Harmon et al., 2019). Green circles indicate crust formed on the North American plate, and yellow is crust formed on South American plate. DAP = Demerara Abyssal Plain. (b) Magnetic anomaly grid. The grid was made as described in Allen et al. (2019) with thin lines in background showing survey tracks used. Magnetic anomalies were identified by extending those of Müller et al. (1999) southward, guided by the synthetic flow lines shown in (a). Magnetic fabric offsets coincide with the fracture zones determined from gravity data. (c) OBS positions (numbered) underlain by EM120 bathymetry contoured every 50 m. Seabed instruments shown in Figure 3 are highlighted in red.

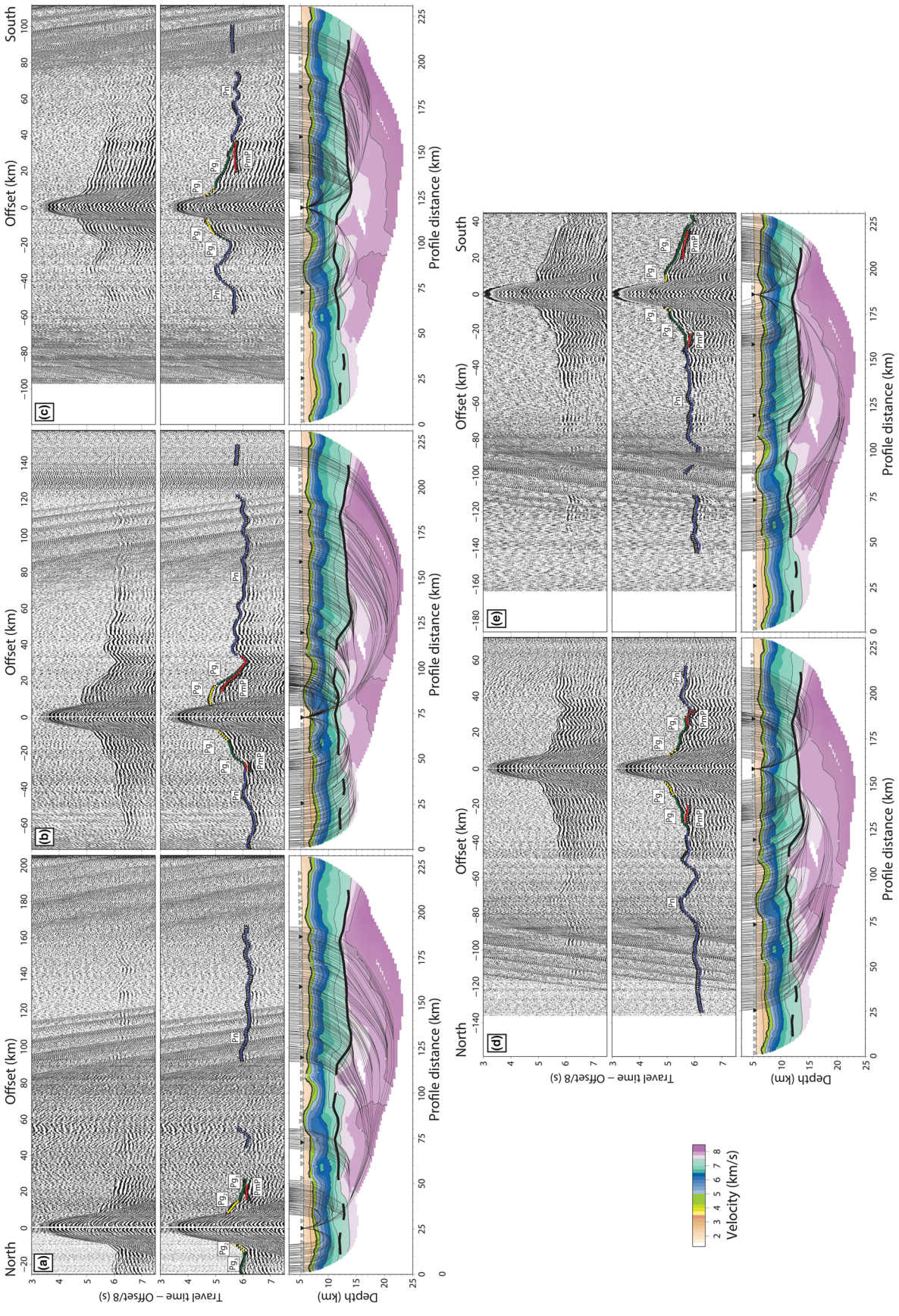

Figure 3. (a) OBS 246, (b) OBS 306, (c) OBS 318, (d) OBS 328, and (e) OBS 335. Top: Receiver gathered data filtered with an Ormsby band-pass filter (3, 5, 10, and 15 Hz). Middle: Receiver gathered data with travel time picks and associated error bars (vertical black lines). Modeled seismic phases through the final model represented by yellow (Pg_2), green (Pg_3), blue (Pn), and red (PmP) circles. Bottom: ray paths through the final velocity model. Inverted triangles show all instruments used in the inversion; black inverted triangles show the instruments shown here; and solid black line represents the Moho interface sampled by PmP reflections.

Table 1
Picking Statistics for All Observed Compressional Phases

Phase	Pick uncertainty (relative to OBS/H)	# of picks	Average pick uncertainty (ms)
Ps	50 ms	1,026	50
PbP	70 ms	503	70
Pg_2	30 ms + 0.25 ms km^{-1}	1,901	33
Pg_3	30 ms + 0.25 ms km^{-1}	4,614	36
Pn	30 ms + 0.25 ms km^{-1}	9,797	48
PmP	50 ms	4,005	50

component) stations with an average spacing of 4 km (Figure 2c). The line was shot with a 13-gun, 5,000 cu. in. (82 L), tuned air gun array that was towed at a depth of 9 m and fired at 60 s intervals, giving a nominal shot spacing of 170 m. Each OBS was corrected for internal clock drift using GPS-synchronized clocks. The OBS recorded continuous data at a frequency of 250 Hz, which were cut into a 60 s SEGY trace for each air gun shot (Figures 3a–3e).

OBS positions were corrected for lateral movement during their descent through the water column. This was achieved using a grid-search method, which minimized the least squares difference between the observed water wave travel times and those calculated to a grid of depth nodes. On average, the instruments are corrected by 370 m relative to their deployment position. A minimum phase Ormsby band-pass filter, with corner frequencies of 1, 3, 15, and 40 Hz, was applied to the receiver gathers. Applying a predictive deconvolution filter improved the clarity of reflections on a limited number of instruments. P-wave arrivals were best observed on the vertical component, which was therefore the primary channel used (Figures 3a–3e).

The multichannel seismic data were collected with a 13-gun, 3,750 cu. in. (62 L) air gun array towed at a depth of 9 m. The array was fired every 20 s, giving a nominal shot spacing of 50 m, and was recorded by a 3-km-long, 240-channel hydrophone streamer, towed at a depth of 8 m. The data were processed using the ProMAX software package. Processing included CDP binning at 6.25 m spacing; band-pass filtering (2, 8, 40, and 70 Hz); a minimum phase predictive deconvolution filter (200 ms operator length); a spherical divergence amplitude correction; and finally, a prestack Kirchhoff time migration.

3.2. Phase Identification

Phase identification was assisted by preliminary travel time modeling of first arrivals using the RayInvr and TOMO2D codes of Zelt and Smith (1992) and Korenaga et al. (2000), respectively (Figures 3a–3e). Sediment refractions (Ps) are not observed as first arrivals but are present as secondary arrivals on a few instruments, with apparent velocities of 2.1–2.4 km s^{-1} (supporting information Figure S1). First arrivals, outside of the direct water wave, are composed of refractions from the oceanic crust (labeled as Pg_2 and Pg_3 in Figures 3a–3e) and the mantle (Pn). Pg_2 arrivals have high amplitudes with highly variable apparent velocities owing to the basement topography. These refractions were picked at offsets between 2.5 and 20.5 km. Pg_3 refractions were distinguished from Pg_2 refractions by a decrease in seismic amplitude, a change in apparent velocity, or both. Pg_3 arrivals were picked at offsets between 8.0 and 44.5 km. Moho reflections (PmP) have strong lateral variations in time and are often spatially limited. They were identified where they form clear triplications (e.g., Figure 3c, south) and have increased seismic amplitude (e.g., Figure 3b). Mantle refractions (Pn) were primarily identified by an apparent velocity exceeding 7.6 km s^{-1} and were picked at offsets between 12.5 and 165 km.

Basement topography between 75 and 120 km profile distance causes significant lateral variations in arrival times (e.g., Figures 3b and 3c) and has resulted in out-of-plane reflections in some receiver gathers. Preliminary modeling with iterative pick reclassifications allowed us to correctly identify these phases. For example, OBS 318 shows clear lower crustal arrivals and a triplication to the south, whereas arrivals to the north through basement topography make it difficult to identify a clear PmP arrival (Figure 3c).

For all first arrivals, picking uncertainties were assigned based on their offset from the recording OBS. Secondary (e.g., Ps and PmP) arrivals were given a constant uncertainty of 50 ms (Table 1).

4. Modeling

4.1. Sedimentary Layer

A sedimentary starting model for the tomographic inversion was built from bathymetric and MCS reflection data. Seafloor depth nodes were assigned every 500 m, and the water column was given a fixed compressional velocity of 1.52 km s^{-1} based on measured sound velocity profiles. The top basement horizon was picked from the prestack Kirchhoff time-migrated reflection image along the profile and converted to depth using an average velocity of 2.25 km s^{-1}, based on stacking velocities. Basement depth nodes were defined

Table 2
Misfit Statistics Through Final TOMO2D Velocity Model for All Identified Seismic Phases

Phase	Travel time picks	Misfit (ms)	Chi-square (χ^2)
All	16,311	44	0.85
Pg_2	1,901	31	0.93
Pg_3	4,614	30	0.73
Pn	9,796	47	1.03
PmP	4,051	55	1.19

every 1 km throughout the model. Velocities of 2.1 and 2.4 km s^{-1} were initially assigned to the top and base of the sediments, respectively. Secondary sediment refraction arrivals (Ps) and reflections from the top basement (PbP) recorded by the OBS data (Figure S1) were forward and inverse modeled using the RayInvr code of Zelt and Smith (1992). The final sedimentary velocity model has an RMS travel time misfit of 51 ms and a chi-square (χ^2) value of 1.14 with velocities increasing from ~2.0 km s^{-1} at the seafloor to 2.9 km s^{-1} at the deepest point.

4.2. Tomographic Inversion

Tomographic modeling of the crust and upper mantle structure was performed using TOMO2D (Korenaga et al., 2000). This method determines a 2-D velocity field by simultaneous inversion of first-arrival travel times and reflected arrivals from a single interface. The input velocity model is defined by a sheared mesh, which is hung from the seafloor, with nodes every 500 m in the horizontal direction, and a vertical node spacing smoothly increasing from 25 m at the seafloor to 500 m at the base of the model ~25 km below the seafloor. The shallow structure is taken from the previously described sediment velocities, below which a starting model of a basic oceanic crustal velocity structure is defined, increasing from 4.7 km s^{-1} at top basement to 6.5 and 7.3 km s^{-1}, 2.0 and 7.0 km below top basement, respectively. Velocities in the mantle increase smoothly to 8.5 km s^{-1} at the base of the model (~25 km below the seafloor). The velocity of 4.7 km s^{-1} for the top basement has been chosen based on the observed apparent velocities of refracted arrivals from the uppermost crust. A preliminary floating reflector to simulate the Moho was placed at 12 km depth, with node points defined every 1 km.

Comprehensive testing determined regularization parameters that produced a simple, geologically reasonable model with a low misfit to the observed data. Horizontal correlation lengths increase from 3 km at the seafloor to 16 km at 25 km depth, and vertical correlation lengths increase from 0.5 km at the seafloor to 2.3 km at 15 km depth, below which they remain constant. A constant correlation length of 5 km was used for the depth of the Moho reflector. A depth weight kernel of 1.0 was used, giving an equal weighting between velocity and interface depth perturbations. A top-down inversion strategy was employed, first inverting for upper crustal refractions (Pg_2), followed by the combined inversion of all crustal refractions and PmP reflections (Pg_2, Pg_3, and PmP), and finally an inversion with the addition of mantle refractions (Pg_2, Pg_3, PmP, and Pn). At each stage, 10 inversion iterations were run. In each subsequent set of inversions, a variable damping is applied, defined by the ray coverage of the previous model step, in order to favor velocity perturbation in the deeper model regions.

Figures 3a–3e show selected receiver gathers with picked and calculated seismic arrivals. The final model has an overall RMS travel time misfit of 44 ms and χ^2 value of 0.85 (Table 2).

4.3. Uncertainty Analysis and Quality Checks

4.3.1. Monte Carlo Uncertainty Analysis

Error can be introduced into the tomographic inversion in many ways, including uncertainty in travel time picks and characteristics of the starting model. In order to quantitatively assess this, Monte Carlo uncertainty analysis was performed. Randomized timing errors were added to the travel time data to produce 100 unique noisy travel time data sets. This includes a common receiver error (± half the maximum pick error recorded on each OBS), which accounts for uncertainties arising from the instrument relocation, offline distance and timing issues, and picking errors (± half the individual pick error). One hundred randomized starting models were generated by modifying the initial 1-D oceanic crustal structure hung below the sediment model. Velocities at the top and bottom of the upper and lower crust, as well as top mantle, were randomized by ±5% of the original starting velocity, while the depths of the boundaries in the 1-D model were randomized by ±10% in each new model generated. The randomized travel time data and starting model pairs were inverted using the original inversion scheme and parameters described in section 4.2. Through these inversions, the array of starting models converges toward a common solution. The mean model from these realizations (Figure 4a) is used in the following results and discussion. The standard deviation of the solutions gives a measure of the modeling uncertainty (Figure 4c).

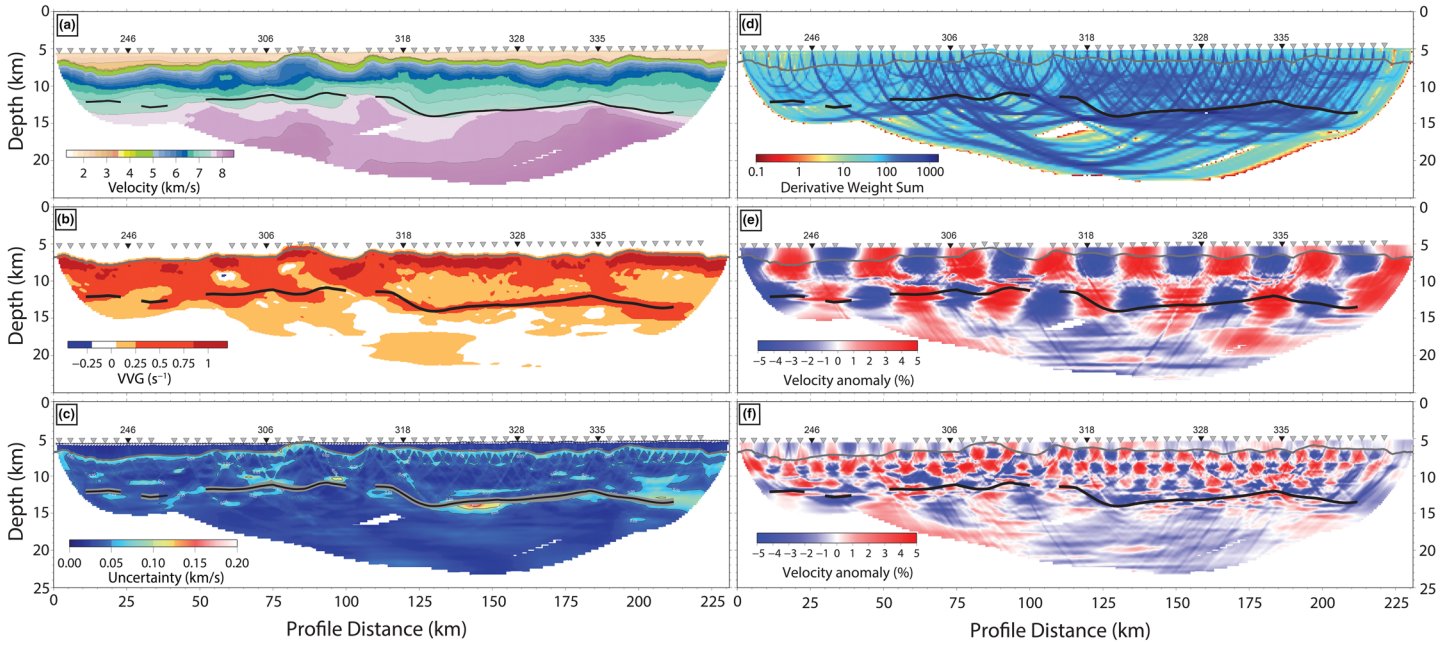

Figure 4. (a) Final velocity model. This is the mean from 100-individual inversion realizations. Inverted gray triangles show the location of OBS. Black inverted triangles indicate receiver gathers in Figure 3. Thick black line represents the averaged Moho reflection from the Monte Carlo process. (b) Vertical velocity gradient of the final model, below top basement, highlighting different modes of crustal accretion. A smoothing of 1 km is applied. Gray line is the location of top basement. (c) Monte Carlo velocity uncertainty in the average velocity model, taken as the standard deviation of the 100-individual inversion realizations. The standard deviation of the Moho surface is indicated with the light gray envelope. (d) Ray coverage through the final velocity model, represented by the derivative weight sum. (e) Checkerboard result showing the recovery of velocity anomaly checks that have dimensions of 15.0 × 5.0 km. (f) Checkerboard result showing the recovery of velocity anomaly checks that have dimensions of 5.0 × 2.5 km.

Throughout most of the model, the uncertainty in the resolved velocity is less than 50 m s^{-1}. Velocities at the top of basement typically have higher uncertainty (60–80 m s^{-1}), likely due to a lack of first-arrival turning waves from this depth (~5–8 km, Figures 3a–3e and 4c–4e). The largest uncertainties in the model are in the upper mantle at 140–155 km profile distance, where it reaches 155 m s^{-1}. This area of uncertainty may be associated with discontinuous and uncertain PmP reflection/mantle refraction picks. However, this higher uncertainty only exists over a limited spatial extent. Through all the inversion realizations, the maximum deviation of the Moho reflection is 300 m, while the standard deviation is 110 m, indicating that the model is very robust.

4.3.2. Ray Coverage

Ray coverage through the final model is represented by the derivative weight sum (Figure 4d). There is excellent ray coverage through the sediment, crust, and upper mantle between 50 and 225 km profile distance. Ray coverage directly below the resolved PmP reflector is excellent, and many of the shorter offset mantle arrivals may have traveled as head waves. A small gap in ray coverage at 16 km depth, between 105 and 120 km profile distance, could be due to ray focusing from basement and Moho topography between 80 and 130 km profile distance. The ray coverage (DWS > 0) is used to mask the final velocity model, and quality checks (e.g., checkerboard tests and uncertainty analysis), to show only regions sampled by seismic data.

4.3.3. Checkerboard Testing

Checkerboard resolution tests were performed to determine the size of structures resolvable in the final velocity model (Zelt & Barton, 1998). Sinusoidal velocity perturbations of ±5% were introduced into the final velocity model for a range of anomaly dimensions. Synthetic travel times were calculated through each perturbed model using the forward ray tracing method, with random noise added using the same method as described in the Monte Carlo uncertainty analysis. These noisy travel time data sets are then inverted with the same input model and inversion parameters as our original inversion scheme. The recovered anomalies are the difference between these results and the final velocity model.

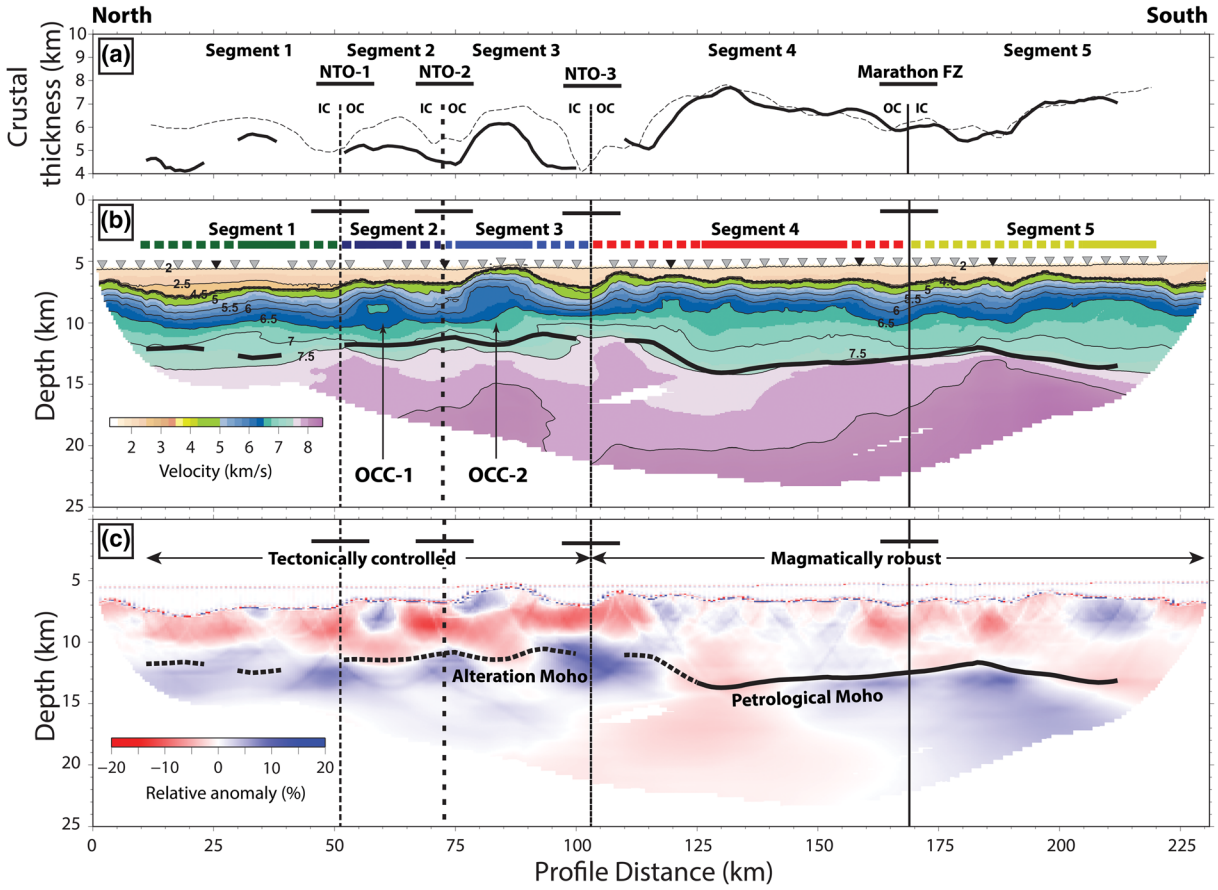

Figure 5. Determining crustal domains. (a) Crustal thickness as measured between top basement and the tomographically determined PmP reflector (solid black line) and the 7.5 km s^{-1} velocity contour (thin dashed black line). Horizontal black bars show the location of crustal discontinuities determined from potential field data (±5 km uncertainty). IC and OC refer to the inside and outside corners, respectively, as determined from magnetic offsets (Figure 2b). (b) Final velocity model. Solid horizontal colored bars indicate the center of the segments, and dashed horizontal colored bars indicate the ends of the segments. Colors correspond to the 1-D velocity profiles seen in Figure 6. Vertical lines indicate the location of 1-D velocity profiles through crustal discontinuities, seen in Figure 6f. Other details as in Figure 4. (c) Velocity anomaly computed by subtracting the average 1-D crustal structure. Dashed black line indicates where PmP reflection originates from a serpentinization front.

We used check dimensions of 5–30 km laterally and 2.5–10 km vertically. Figure 4e shows the excellent recovery of 15 × 5 km checks throughout the crust and uppermost mantle, while Figure 4f shows the high recovery of anomalies with dimensions of 5 × 2.5 km through the crustal section. There is some diagonal smearing of the recovered anomalies at the northern and southern extremes of the profile, likely due to unidirectional ray coverage. Anomalies below 15 km depth are poorly resolved or not resolved at all.

5. Results

The final velocity model is shown in Figure 5b together with the locations of the ridge discontinuities determined from potential field data as discussed in section 2 (black horizontal bars, Figure 5). While there is a small mismatch at the Marathon FZ, which may be due to uncertainties in the potential field data, overall, the resolved PmP reflection shallows toward each of these discontinuities over tens of kilometers. Figure 5c shows velocity anomalies relative to the average 1-D velocity structure along the profile (black line, Figures 6a–6e). Segment centers (colored horizontal bars, Figure 5b) show a relatively high-velocity upper crust and low-velocity lower crust (blue above red, Figure 5c), or no anomaly at all (white). Segments 2 and 3 have the most pronounced relative seismic anomaly. The segment ends and ridge discontinuities (dashed colored horizontal bars, Figure 5b) have relatively low upper crustal velocities and high lower crustal velocities (red above blue, Figure 5c). A set of velocity-depth profiles for each of the segments is shown in

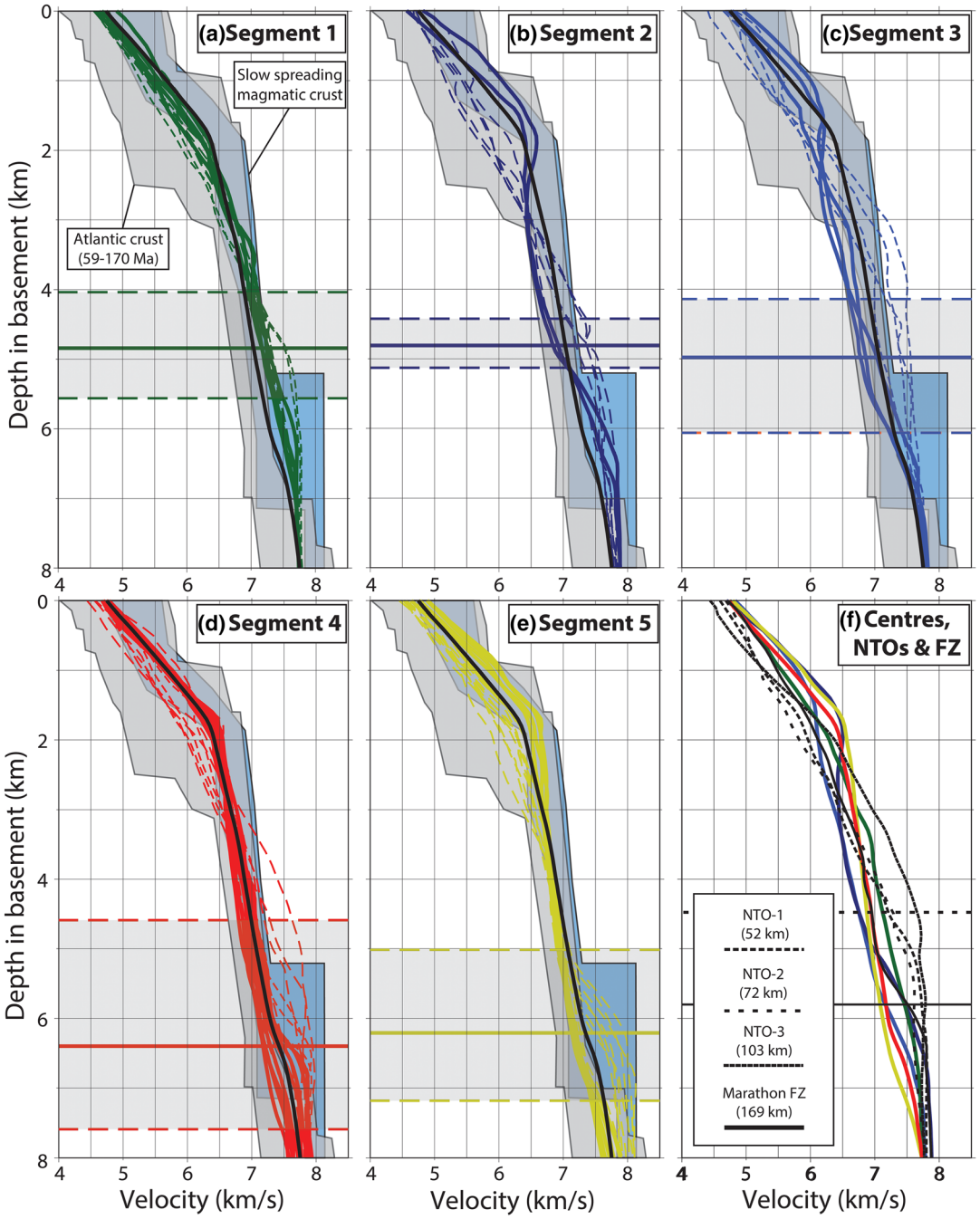

Figure 6. (a–e) Velocity-depth profiles by segment, extracted every 4 km through the final velocity model compared with previous compilations of oceanic crustal structure. Solid color lines are 1-D profiles from the segment centers and dashed color lines from the segment ends (see Figure 5b for locations). Black line represents average through entire model used to derive Figure 5c. Light gray shading is velocity envelope from White et al. (1992) for Atlantic oceanic crust aged 59–144 Ma. Light blue shading is the velocity envelope from Christeson et al. (2019), for mature (>7 Ma) magmatic slow-spreading crust. Solid horizontal line represents the average depth of the resolved PmP reflections (segment centers and segment ends combined). Horizontal shaded regions represent range of PmP reflection depths throughout the segments. (f) Velocity-depth profiles through the center of fracture zones and nontransform offsets (numbers refer to profile distance) compared with the average through the segment centers. Horizontal lines represent the depth of resolved PmP reflections, where observed in these crustal discontinuities.

Figures 6a–6f and for the discontinuities in Figure 6f. Within the center of the two southern segments (4 and 5), the crust has a well-defined two-layered structure. Velocities in the upper crust increase from 4.8 km s^{-1}, at the top of basement, to 6.4 km s^{-1}, 1.8 km below, giving a velocity gradient of 0.9 s^{-1} (Figures 4b, 6d, and

6e). In the lower crust, velocities increase with a gradient of 0.2 s^{-1} from 6.4 to 7.3 km s^{-1} over a 4.4 km depth interval. In contrast, velocities within the centers of the three northern segments (1–3) vary significantly from the average 1-D structure and are discussed in greater detail in the following sections. The velocity profiles within FZ/NTOs typically increase in a single gradient over 4.2–5.5 km from upper crustal velocities (4.5–4.8 km s^{-1}) to lower crustal/upper mantle velocities (7.3–7.6 km s^{-1}) (Figure 6f). Note that in order to describe the results below, we define the seismic crustal thickness as the distance between top basement and the inverted PmP reflector; this will be revisited within the discussion. Unless otherwise specified, depths are beneath the top of basement. We will first describe the velocity structure within each segment and then the structure of the discontinuities.

5.1. Segment Centers

Segment 4 has a typical velocity structure for oceanic crust aged 59–170 Ma (Figure 6d) (Christeson et al., 2019; White et al., 1992). Uppermost basement velocities (Layer 2) range between 4.6 and 4.9 km s^{-1} and increase to ~6.4 km s^{-1} at ~1.9 km depth, giving a velocity gradient of ~0.9 s^{-1} (Figures 4b and 6d). Below this in Layer 3, velocities increase gradually to 7.1–7.3 km s^{-1} at approximately 6.3–7.3 km depth, giving a reduced velocity gradient of ~0.16 s^{-1}. At the base of Layer 3, the velocity increases from ~7.3 to ~7.6 km s^{-1} over a depth interval of ~500 m (gradient ~0.6 s^{-1}). This is likely a smoothing effect by the tomography code of the lower crust and upper mantle, across the resolved PmP reflector.

PmP reflections are observed throughout Segment 4, albeit with variable strength (Figures 3c–3e), and closely match the 7.5 km s^{-1} velocity contour (Figures 5a and 5b). Overall, the segment has an average seismic crustal thickness of 6.6 ± 1.0 km, with a relatively flat Moho and basement topography between 140 and 165 km. North of this, the seismic crustal thickness increases to as much as 7.6 km, between 125 and 135 km profile distance. In the segment center, velocities below the PmP reflector typically increase from ~7.5 km s^{-1} to normal mantle velocities (>7.8 km s^{-1}) within 1 km.

Segment 5 has a velocity structure that is very similar to that of Segment 4 (Figures 6d and 6e). In its center (200–220 km, Figure 5), Layer 2 is as thin as ~1.8 km, giving a higher-velocity gradient of ~1.0 s^{-1} (Figure 4b). Lower crustal velocities increase to 7.4 km s^{-1} over 4.2–5.2 km, with a velocity gradient of ~0.19 s^{-1}. There are clear and continuous PmP reflections (Figure 3e), which also match the 7.5 km s^{-1} velocity contour. Crust within the center of this segment has an average seismically determined thickness of 6.8 ± 0.3 km, consistent with Segment 4. The mantle structure is also consistent. The structure of the crust at the northern end of Segment 5 has strong similarities to that at the southern end of Segment 4 such that there is a level of symmetry across the Marathon FZ, unlike that seen across NTO-3.

Within the center of Segment 1 (30–42 km, Figure 5b), the seismically determined crust has an average thickness of 5.2 ± 0.4 km. The PmP reflection correlates primarily with velocities of 7.3 km s^{-1}, lower than that of the two southern segments. The crustal velocities also present a much less distinct two-layered structure when compared to the two southern segments (Figures 6a, 6d, and 6e). A constant velocity gradient of 0.8 s^{-1} in the upper crust persists to velocities of ~6.3 km s^{-1} at approximately 1.9 km depth (Figure 4b). Below this, velocities increase to 7.3 km s^{-1} over a depth interval of 3.4 km, giving a velocity gradient for lower crust of ~0.3 s^{-1}. Velocities in the upper mantle increase from 7.3 to 7.8 km s^{-1} over 3–4 km depth interval, giving a velocity gradient of ~0.2 s^{-1}.

Segments 2 and 3 present dome-like basement and velocity structures, centered on 58 and 81 km profile distance, which are markedly different to all the other segments (Figures 5b and 6a–6e). Pronounced basement topography is observed within Segment 3, which rises 1.5 km above the surrounding basement level and even reaches the seafloor (75–95 km, Figure 5b). These features match the structural characteristics of some OCCs observed at the MAR, and forthwith, we refer to them as OCC-1 and OCC-2, respectively (Canales et al., 2007).

OCC-2 is within the center of Segment 3 and has an asymmetric domal structure (Figure 5b). It has high upper crustal velocities of 5.0 km s^{-1} at the top of basement at 75–80 km (Figure 6c), with a velocity gradient of 1.0 s^{-1} (Figure 4b), typical of Layer 2. This is the highest top basement velocity observed along the entire profile. A velocity inversion decreases velocities from 6.2 km s^{-1} at 1.5 km to 6.1 km s^{-1} at 2.5 km depth. This low-velocity zone (LVZ) is present between 78 and 84 km profile distance, deepening by 1.1 km northwards

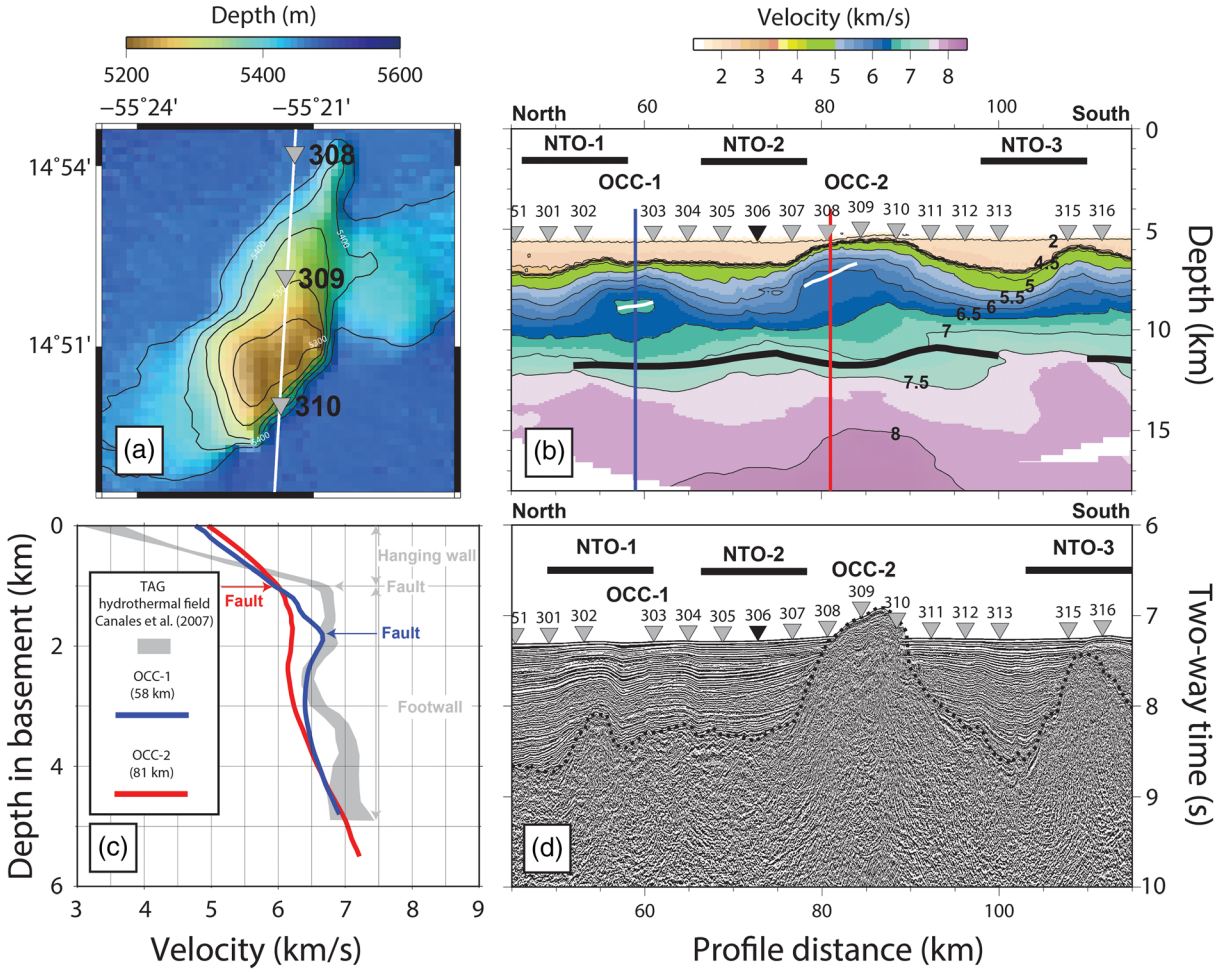

Figure 7. Details of two identified oceanic core complexes. (a) Bathymetry showing the seafloor expression of OCC-2 and OBS used to resolve the seismic structure indicated by numbered gray triangles. (b) Zoom-in of final velocity model showing velocity structure of OCC-1 and OCC-2. White lines indicate the inflection points above the OCC LVZs, which is interpreted to be the location of detachment faulting. Colored lines through the center of the OCC indicate the location of 1-D profiles seen in (c). (c) Velocity-depth functions through OCC-1 and OCC-2, compared with the TAG hydrothermal mound from Profile 1 in Canales et al. (2007). (d) Kirchhoff time-migrated reflection seismic image showing basement configuration in two-way time.

(Figures 4b, 5b, and 7b). From 2.5 to 6.5 km depth, velocities increase to 7.2 km s^{-1} at the PmP reflector, with a velocity gradient of ~0.2 s^{-1} (Figure 6c). Typical mantle velocities (>7.8 km s^{-1}) below OCC-2 are reached 1.9 km below the PmP reflector.

OCC-1 forms a large portion of Segment 2 and is directly south of NTO-1 (50–65 km, Figure 5b). This feature presents the same domal velocity structure as OCC-2. Layer 2 has typical upper crustal velocities and is 1.8 km thick, below which we observe a pronounced velocity inversion, decreasing from 6.7 to 6.4 km s^{-1}, 1.0 km below (Figure 6b). Below this inversion, velocities smoothly increase to 7.0 km s^{-1} at the Moho. Full mantle velocities are reached 1.7 km below the PmP reflector. It should be noted that both LVZs (in OCC-1 and OCC-2) have higher-velocity uncertainties than the surrounding crust ($\pm$0.08 and $\pm$0.06 km s^{-1}, respectively), but these uncertainties are smaller than the magnitude of the velocity decreases. It is likely that these LVZs are smoothed in depth by the modeling and have a more limited depth extent in reality.

5.2. Transform Offset and NTO Structure

Both the transform offset and the NTO in our final velocity model are characterized by shallowing of the PmP reflector and velocity gradients distinct from the segment centers (Figures 4b, 5a, and 5b). The ridge

discontinuities each have a single velocity gradient (Figure 6f), which ranges between 0.6 and 0.8 s^{-1} at the NTOs and 0.5 s^{-1} at the Marathon FZ.

NTO-3 is the most prominent discontinuity in the final tomography model (Figure 5b), with thin crust over a 30-km-wide zone. Despite no positively identified PmP reflections in the center of the discontinuity, if we interpolate the PmP interface through this area, it gives the upper bound on the igneous crustal thickness as 4.2 km. Upper crustal velocities in the center of NTO-3 are 4.4 km s^{-1}, the lowest observed along the profile (Figure 6f). Velocities increase approximately linearly to 7.6 km s^{-1} at 4.2 km depth, giving a velocity gradient of 0.8 s^{-1}.

NTO-1 has less distinct change in crustal thickness than NTO-3, with less shallowing of sparse PmP reflections from Segment 1 to the north (Figure 5b). However, there is a shallowing of the 7.5 km s^{-1} velocity contour from the center of Segment 1 over <15 km toward NTO-1. We infer that the maximum igneous crustal thickness within this discontinuity is ~4.3 km, like NTO-3. Velocities increase smoothly from 4.7 to 7.5 km s^{-1} at 5.0 km depth, with a velocity gradient of 0.6 s^{-1} (Figures 4b and 7).

NTO-2 is unlike the other two NTOs in that we can trace PmP reflections continuously that shoal along strike over 10–15 km to as little as 4.4 km depth. However, these do not seem to be associated with a clear velocity discontinuity but rather lie within a single velocity gradient of 0.6 s^{-1}, from 4.7 km s^{-1} at the top of basement to 7.5 km s^{-1} at 5.0 km depth (Figures 4b and 7).

The medium-offset Marathon FZ is well resolved within the model with continuous Moho reflections, revealing a symmetrical thinning of Layer 3 across the FZ axis (Figures 3d and 3e, 4b–4f, and 5a–5c). The crust thins gradually over 20–25 km, decreasing from 6.6–6.9 km in the neighboring segment centers, to a minimum crustal thickness of 5.3 km. There is a constant velocity gradient of 0.5 s^{-1} to a depth of 5.3 km, lower than that observed in the three NTOs, with velocities increasing from 4.8 to 7.3 km s^{-1}. Below this, there is a relatively sharp increase in velocity over the 5.3–6.3 km depth range, increasing from 7.3 to 7.8 km s^{-1} (Figure 6f). Typical mantle velocities of 7.8 km s^{-1} are reached within 1 km below the PmP reflector.

6. Discussion

6.1. Evidence for Two Types of Crustal Accretion

Previous studies have attempted to define a single two-layered velocity-depth (Penrose) model to represent slow-spreading crust (e.g., White et al., 1992). However, the five ridge segments present two distinct structures within our final velocity model: Two have the classic two-layered structure, and three do not. We interpret these distinct velocity structures as the products of two endmembers of crustal accretion at the MAR: magmatically robust and tectonically controlled. We believe that many previous compilations of slow-spreading oceanic crust have oversimplified the structure by merging the two crustal modes into a generalized velocity-depth envelope (e.g., Grevemeyer, Hayman, et al., 2018; White et al., 1992). A recent compilation of slow-spread oceanic crust by Christeson et al. (2019) excludes "anomalous" regions, including oceanic-core complexes, LVZs, crustal discontinuities, and zones interpreted as serpentinized. While this analysis gives a more accurate model of the magmatic accretion, it inherently excludes multiple settings observed at the ridge axis.

Within the center of Segments 4 and 5 (Figures 4b, 5b, 6d, and 6e), the upper crust is 1.8–1.9 km thick with a high-velocity gradient (~0.9 s^{-1}), overlying lower crust with a much lower velocity gradient (~0.2 s^{-1}) and an average thickness of 5.0 $\pm$ 0.8 km. The PmP reflector coincides with the 7.5 km s^{-1} contour, and velocities increase to >7.8 km s^{-1} within ~1 km below, suggesting it is a petrological boundary between crust and mantle (Figure 5c) (Lizarralde et al., 2004). Overall, the centers of these segments have an igneous crustal thickness of 6.8 $\pm$ 0.8 km, close to the global average (Christeson et al., 2019; White et al., 1992). These segments are therefore consistent with the classic Layer 2/3 Penrose model of oceanic crust, and we interpret them as being magmatically robust. They also show an excellent agreement with the velocity envelope for mature, slow-spreading magmatic crust from the compilation of Christeson et al. (2019). Crustal thinning toward their ends agrees well with the concept of melt delivery focused to the segment centers, with less magma supplied to the segment ends (e.g., Dunn et al., 2005; Hooft et al., 2000; Hosford et al., 2001; Lin & Phipps Morgan, 1992; Minshull et al., 2003; Phipps Morgan &

Chen, 1993; Tolstoy et al., 1993). At the current MAR, spreading segments with these seismic characteristics are widely reported, including the Lucky Strike segment (Seher et al., 2010), the OH segments south of the Oceanographer FZ (Canales et al., 2000; Dunn et al., 2005; Hooft et al., 2000), segments south of the Kane FZ (Dannowski et al., 2010), crust neighboring the TAG hydrothermal area (Canales et al., 2007), the segment between the Mercurius and Marathon transforms (Peirce et al., 2019), and segments north of the 5°S FZ (Planert et al., 2009).

Conversely, the centers of Segments 1–3 do not have this well-defined two-layer velocity structure (Figures 4b, 5b and 5c, and 6a–6c) and are more variable than the magmatic segments. The PmP reflector corresponds to velocities of 7.0–7.2 km s^{-1}, and whether we define the crustal thickness by the PmP reflector or the 7.5 km s^{-1} contour, the crust is thinner than in Segments 4 and 5 (Figure 5a). Midcrustal to lower crustal velocities fall outside the envelope for mature magmatic ocean crust (Christeson et al., 2019), while PmP reflections occur at shallower depths (Figures 6a–6c). We therefore interpret Segments 1–3 as having an overall lower magmatic budget than Segments 4 and 5 and being tectonically controlled as described in the Chapman model of oceanic crust. Seismic velocities observed at midcrustal and lower crustal depths in Segments 2 and 3 are lower than those in the remaining segments (Figures 5c and 6f). We attribute this velocity reduction to normal faulting in the upper crust to midcrust, which opened fractures and allowed hydrothermal circulation and alteration to depth (Canales, Detrick, et al., 2000; Hooft et al., 2000; Hosford et al., 2001; Minshull et al., 2003; Planert et al., 2009; Seher et al., 2010). The more gradual gradient from "crustal" to "mantle" velocities in these segments could be due to an intermix of rock types. PmP reflections are often not observed within OCC, and it has been suggested that this could be the result of a magma deficit at the time of accretion or gradational serpentinization, which lowers the velocity of upper mantle peridotites to that of gabbros (Blackman et al., 2009; Dunn et al., 2017; Peirce et al., 2019; Zhao et al., 2012). A further characteristic of Segments 2 and 3 is local velocity inversions, which we interpret as OCCs as discussed in section 6.4.

Heterogeneous crustal velocity structures have also been reported in recent seismic studies of the MAR, including at the Rainbow Massif (Canales et al., 2017; Dunn et al., 2017; Paulatto et al., 2015), the Atlantis Massif (Blackman & Collins, 2010; Canales et al., 2008), the TAG hydrothermal mound (Canales et al., 2007; Zhao et al., 2012), the Kane OCC (Canales, 2010; Xu et al., 2009), crust at 22°19′N (Dannowski et al., 2010), and the spreading segments immediately north of the Marathon Transform (Peirce et al., 2019). At those locations, it is possible to place the velocity structures in a broader context of the basement morphology, due to the lack of sediment. These heterogeneous structures coincide with widespread faulting, large throw detachment faults, and the exposure of corrugated massifs associated with OCCs, showing the relative dominance of tectonic processes.

While the velocity-depth profiles within both types of seafloor spreading segment show a fit within the generalized envelopes of previous compilations (gray and light blue shading in Figure 6), this gives a false impression of relatively homogeneous structures and processes. Instead, we have found two distinct seismic structures that are consistent with the two modes of oceanic crustal accretion observed at the modern MAR. The different structures persist as the crust matures, and so its ability to buffer volatiles, such as carbon and water, will vary spatially. Within our final model, segments interpreted as magmatically robust comprise 56% of the total line length. Observations at the MAR between 12.5°N and 35°N suggest that detachment faulting occurs along 50% of the axis (Cann et al., 2015; Escartin et al., 2008; Smith et al., 2006). Taken together, this implies that only around half of the seafloor of the Atlantic, formed at a slow-spreading rate, is made of classic "Penrose-type," layered magmatic oceanic crust, as observed in previous studies (Cann et al., 2015).

6.2. Nature of the Crust-Mantle Boundary

The two types of crustal accretion generate PmP reflectors with different characteristics. Within magmatically robust segments, the reflector corresponds to the 7.5 km s^{-1} contour, and there is a rapid increase to normal mantle velocities >7.8 km s^{-1} below. Hence, we interpret the Moho here as a simple petrological boundary between crust and mantle. A sharp velocity contrast, which is expected for such a boundary, is not resolved within the velocity model given the tomographic smoothing. However, the rapid increase to mantle velocities over a depth range of ~1 km, half that of the vertical correlation length at this depth, is evidence for a sharp transition. In contrast, within the tectonically controlled segments, the PmP reflector

occurs where velocities are 7.0–7.2 km s^{-1} and is underlain by a further gradient over 3–4 km until normal mantle velocities are reached. This could be interpreted in three ways. (1) Deformation and alteration of a shallower petrological Moho has erased the strong velocity contrast across this boundary, and PmP reflections instead originate from a serpentinization front within the upper mantle (Figure 5c) (Minshull et al., 1998; Escartín et al., 2003; Delescluse et al., 2015). (2) The PmP reflector may still be a petrological boundary between mafic and ultramafic material, but deep fracturing and alteration has lowered velocities on either side of this boundary. The drilling results from IODP Site 1309 at Atlantis Massif show that a similar degree of alteration causes greater reduction of seismic velocities within olivine-rich rocks than in typical oceanic gabbros (Blackman et al., 2019). Hence, the mantle rocks beneath the PmP reflector could have undergone a larger velocity reduction than the mafic rocks above. (3) Crust in tectonic segments is formed of gabbroic plutons, hosted in an ultramafic matrix, which become volumetrically less abundant at greater depth, often referred to as the "plum pudding" model (Cannat, 1993; Ildefonse et al., 2007). Moho reflections may not be expected in this setting given a gradual increase in seismic velocity, with some authors suggesting that such settings would still require a serpentinization front in order to generate the observed seismic reflection (Minshull et al., 1998). Nevertheless, phases that behave like wide-angle reflections can still be generated within zones of steeper gradient, even without a discontinuity. While we do not favor any one interpretation for the generation of PmP reflections in tectonic segments, each interpretation requires the alteration of mantle peridotites, mafic material, or both, unlike the petrological Moho in the magmatic segments.

6.3. The Structure and Role of Second-Order Discontinuities

Compiled seismic studies of Atlantic FZs (Detrick et al., 1993) and of geophysical and geochemical observations at the ridge axis (Carbotte et al., 2016) both suggest that the structure of the first- and second-order discontinuities is similar and independent of the size of the ridge offset. This conclusion is supported by our results; we argue below that the accretion state (magmatic vs. tectonic) of the neighboring segments is a more significant factor in determining the crustal structure variations than the offset and geometry of the discontinuity.

Our final velocity model shows a marked shallowing of the PmP reflector over distances >10 km toward the ends of both magmatic segments (Figure 5). The thinning of Segment 4 is strongly asymmetric: The northern end thins by 3.4 km over ~18 km (192 m km^{-1}), while the southern end thins more gradually by 1.3 km over ~24 km (54 m km^{-1}). Such asymmetry has previously been attributed to the offset geometry, with more rapid thinning at the inside corner than the outside corner (e.g., Canales, Detrick, et al., 2000, for the OH-1 segment at the MAR; Figure 1). However, this cannot be the case for Segment 4, which has two outside corners (Figure 5a). Instead, the rapid thinning end abuts a tectonic segment and the more gently thinning end a magmatic segment. Similarly, crustal thinning across the Marathon FZ, which separates two magmatic segments, is symmetric despite being composed of one inside and one outside corner. Therefore, we suggest that the thinning toward segment ends is controlled primarily by the nature of the neighboring segments.

Within each of the discontinuities, we observe single velocity-depth gradients between 0.5 and 0.8 s^{-1} (Figure 6f). At the NTOs, the gradient continues until mantle velocities (>7.8 km s^{-1}) are reached. We interpret this as decreasing fracturing and/or serpentinization of upper mantle peridotites with depth, potentially with a thin overlying igneous crust (Minshull et al., 1998). While there is still a PmP reflection beneath NTO-2, similar observations have been made at the Atlantis II Transform and Labrador Sea spreading center and are interpreted as serpentinization boundaries (Delescluse et al., 2015; Minshull et al., 1998). The lack of PmP beneath NTO-1 and NTO-3 may indicate that the variations are very gradual or that any boundaries have structure too complex to produce coherent reflections with our wavelengths (e.g., Larkin & Levander, 1996). In contrast, the Marathon FZ shows a lower velocity gradient of 0.5 s^{-1}, which steepens beneath 5.5 km depth to reach mantle velocities by 6.5 km, with clear PmP reflections. This difference, and correspondingly lower velocities from 2–6 km depth, may reflect that the larger offset (60 km) and longer activity (2.6 Myr) of the fault have increased fracturing and serpentinization. Alternatively, given the location between two magmatically robust segments, this may indicate the presence of gabbro intrusions even within the FZ. In both segment types, going from the segment center toward the discontinuity, mid-crustal velocities decrease, and the contrast in the velocity gradients between the upper and lower crust

diminishes (dashed lines in Figure 6). Similar patterns have been previously reported at the MAR, for example, toward the ends of the OH-1 (Hooft et al., 2000) and Lucky Strike (Seher et al., 2010) segments, where they were attributed to increasing tectonization of the crust. However, we are now able to distinguish that the magmatically robust Segments 4 and 5 maintain velocities and gradients characteristic of Layer 3 through the transition, with continuous PmP indicating that a petrological crust-mantle boundary is maintained, whereas the tectonically dominated Segments 1–3 develop a single gradient approaching, but still outside, the discontinuity, suggesting a gradual transition from igneous crust to tectonized and altered peridotite.

This changing nature of the Moho, pattern of crustal thinning and velocity structure is consistent with the previously interpreted interplay between tectonism and available magma at slow-spreading ridges (Cann et al., 2015; Olive et al., 2010; Planert et al., 2009; Tucholke et al., 2008). Planert et al. (2009) observed that crust formed in times of reduced melt flux exhibits extreme thinning from the segment centers to the bounding transforms (8.5 to <3.0 km), primarily accommodated by the thinning of Layer 3. In contrast, crust formed during periods of elevated melt flux shows little thinning at the segment ends and maintained the Layer 2/3 structure across crustal discontinuities. Our results also show the strong control of bulk magma flux on the structure of the segments and their ends. During periods of lower melt supply, the already thin segment centers thin further toward the segment ends, where there is little evidence of Layer 3 velocities (e.g., Segments 1–3 and NTO-1–NTO-3). Magmatic periods result in more limited crustal thinning toward the discontinuities, and Layer 3 velocities persist through these segment ends (e.g., Segments 4–5 over the Marathon FZ).

6.4. Oceanic Core Complexes in Mature Atlantic Oceanic Crust

Studies at the MAR axis have shown that in the case of extreme tectonic extension, low-angle detachment faults form, which can cross-cut the entire crustal section, and both exhuming lower crust and upper mantle materials (Canales et al., 2007; Dannowski et al., 2010), and providing fluid pathways (Blackman et al., 2019; Harding et al., 2017). Identification of OCCs at the MAR relies primarily on recognizing corrugated massifs by bathymetric mapping (e.g., Cann et al., 1997; Smith et al., 2008). The subsurface of some OCCs has been investigated to determine their internal structure, formation, and early evolution, for example, TAG hydrothermal mound and Atlantis Massif (Blackman et al., 2019; Canales et al., 2007; Canales et al., 2008; Henig et al., 2012), while microseismicity can also provide constraints on fault geometries and activity (e.g., deMartin et al., 2007; Parnell-Turner et al., 2017). However, as these systems age and move away from the ridge axis, sediment eventually shrouds them, making their identification problematic. On our ridge-parallel profile, we interpret two prominent domal structures with lateral dimensions of 15–20 km as OCCs. OCC-2 still has a bathymetric expression (Figure 7a), which, given the scale and orientation of the outcrop, provides additional evidence that this feature is anomalous crust and is most likely an OCC. As well as matching the overall dimensions of OCCs at the MAR, as we will discuss below, these OCCs possess similar seismic velocity characteristics. While off-axis OCCs have been identified in mature crust using bathymetric (e.g., Ohara et al., 2001) and reflection imaging (e.g., Reston et al., 2004; Reston & Ranero, 2011), few have been identified using seismic refraction methods. Delescluse et al. (2015) identified an OCC at the extinct ultraslow Labrador Sea spreading center using tomographic imaging, where serpentinized mantle velocities were observed beneath just 1.5 km of basement. Grevemeyer et al. (2018) produced P-wave and S-wave velocity models of bathymetrically identified OCC in crust aged ~7 Myr old at the ultraslow Mid-Cayman Spreading Centre. These results revealed that OCCs present high Vp/Vs ratios in the shallow crust, associated with crustal-scale detachment faulting and the exhumation and serpentinization of mantle peridotites. Our new OCC observations enable us to compare their velocity structures with the on-axis examples and to draw basic conclusions about the aging processes of these enigmatic features.

Both OCCs have an upper crust with a seismic velocity gradient like the rest of the profile (Figures 6 and 7c). Deeper, there is a marked reduction in velocity gradient, followed by an LVZ. Overall, these velocity-depth structures resemble that found at the TAG hydrothermal mound (Figure 7c) (Canales et al., 2007). While the upper gradient is significantly lower than at TAG, we attribute this to the normal aging processes like the rest of the line. At TAG, Canales et al. (2007) interpret the break in velocity gradient as the detachment fault zone, based on clustering of microseismicity, with a hanging wall composed of upper crustal material,

juxtaposed against a lower crustal footwall below. The different upper crustal thicknesses at the two OCCs in our model (1.8 and 1.0 km, respectively) thus imply different depths to the detachment. In particular, at OCC-2, this is much thinner than Layer 2 elsewhere on the profile, and we interpret the basement reaching the seabed as a rafted block equivalent to that identified by Smith et al. (2008).

LVZs are reported in the seismic structure of the Kane OCC (Canales, 2010) and TAG hydrothermal mound at the MAR (Canales et al., 2007; Zhao et al., 2012), and Mt Dent at the ultraslow-spreading Cayman Trough (Harding et al., 2017). Both Zhao et al. (2012) and Harding et al. (2017) suggest that these LVZs could result from a combination of thermal, lithological, mechanical, or hydrothermal processes that act to reduce the seismic velocity in the footwall. Rotation and uplift of the detachment footwall would result in fracturing and faulting propagating through the footwall, which in turn enables hydration and alteration at depth. Recent drilling of Atlantis Massif shows that intense shallow alteration reduces P-wave velocities in the gabbro footwall from 6.5 to 6.0–6.4 km s^{-1}, up to 800 m below the OCC detachment fault surface (Blackman et al., 2019), consistent with the velocity structure of the upper footwall in our OCC-2. Further evidence of this comes from seismic studies of OCC in the Parece Vela back-arc basin, where shallow reflections are suggested to be generated by localized fracturing and alteration of the gabbroic core (Ohara et al., 2007). The higher midcrustal velocities at OCC-1, relative to OCC-2, may indicate that seafloor exposure and alteration were more limited. Alternatively, the differences may show heterogeneous footwall compositions. Some OCC footwalls may comprise mantle peridotites hosting gabbroic plutons (Dick et al., 2008; Ildefonse et al., 2007), and mixed lithologies could also produce a velocity inversion.

7. Conclusions

Here, we have presented a high-resolution P-wave wide-angle seismic study over ~60–75 Ma Atlantic Ocean crust using 54 OBS, at 4 km spacing along a 225 km profile. Our velocity model spans five crustal segments separated by one FZ (former transform fault) and three NTOs. Our primary findings are as follows:

- Two types of segments have distinctive seismic velocity structures. One has a classic two-layer velocity structure with a high-velocity gradient Layer 2 (~1.0 s^{-1}) above a lower velocity gradient Layer 3 (~0.2 s^{-1}). In such segments, a deep reflector (PmP) coincides with the 7.5 km s^{-1} contour and an increase to >7.8 km s^{-1} velocities <1 km below, defining an average crustal thickness of 6.8 ± 0.8 km. We interpret these segments as dominated by magmatic processes, with PmP representing a petrological boundary between crust and mantle. The other type has a much reduced velocity gradient contrast between the upper and lower crust, with localized seismic velocity inversions, and a PmP reflector shallower than the 7.5 km s^{-1} contour. We interpret these segments as tectonically dominated, with PmP reflections originating from velocity contrasts in, or across, altered mafic and/or ultramafic materials. Along the profile, the two segment types are present in approximately equal proportions, consistent with the modern observations of crustal accretion at the MAR. Our results question the validity of assigning a single 1-D velocity-depth envelope to slow-spread oceanic crust.
- The seismic structures of the NTOs and the FZ segment are similar, despite different ridge offsets. At both types of discontinuity, the PmP reflector shallows by up to 3.1 km over distances >15 km, and a linear velocity gradient between 0.5 and 0.8 s^{-1} is found. Both orders of discontinuity present major boundaries to magmatic and tectonic processes at the MAR. Clear PmP reflections at the ends of magmatic segments indicate that the lithological boundary between crust and mantle is maintained toward the discontinuity. In contrast, at the ends of tectonic segments, PmP is generally missing altogether, which suggests a more heterogeneous lower crustal structure and/or a gradational decrease in fracturing and alteration with depth, both of which act to reduce or eliminate the impedance contrast. The accretion state (magmatic versus tectonic) of the neighboring segments is a more significant factor in determining variations in the crustal structure than the offset and geometry of the discontinuity.
- We have made the first wide-angle seismic identifications of buried OCCs in mature (>20 Ma) Atlantic Ocean crust. Their dimensions and seismic structure are comparable to those studied at the modern MAR. These OCCs show a ~20-km-wide "domal" morphology, with shallow basement

and increased upper crustal velocities relative to normal ocean crust. Seismic velocity inversions are interpreted to be caused by alteration and rock-type assemblage contrasts beneath a crustal-scale detachment fault.

Appendix A: Project Associates

A.1. VOILA Group Consortium

Andreas Rietbrock[3,4], Saskia Goes[1], Jon Blundy[5], Nick Harmon[2], Catherine Rychert[2], Colin G. Macpherson[6], Jeroen Van Hunen[6], Mike Kendall[7], Jamie Wilkinson[1,8], Jon Davidson[6], Marjorie Wilson[9], George Cooper[5], Benjamin Maunder[1], Lidong Bie[4], Stephen Hicks[1,2], Robert Allen[1], Ben Chichester[2], Stephen Tait[10], Richie Robertson[11], Joan Latchman[11], and Frank Krüger[12]

[1]Department of Earth Sciences and Engineering, Imperial College London, UK

[2]Ocean and Earth Science, National Oceanography Centre Southampton, UK

[3]Geophysical Institute, Karlsruhe Institute of Technology, Karlsruhe, Germany

[4]Department of Earth Ocean & Ecological Sciences, University of Liverpool, UK

[5]School of Earth Sciences, University of Bristol, UK

[6]Department of Earth Sciences, Durham University, Durham, UK

[7]Department of Earth Sciences, University of Oxford, UK

[8]Department of Earth Sciences, Natural History Museum, London, UK

[9]School of Earth and Environment, University of Leeds, UK

[10]Institut de Physique du Globe de Paris, Jussieu, Paris, France

[11]Seismic Research Centre, The University of West Indies, Trinidad & Tobago

[12]Institute of Earth and Environmental Sciences, University of Potsdam, Germany

A.2. JC149-leg 3 Science Party

Jenny Collier[1], Tim Henstock[2], Robert Allen[1], Sophie Butcher[1], Gabriella Castiello[3], Chen Chen[2], Caroline Harkin[4], Dan Posse[2], Ben Roche[2], Anna Bird[5], Andy Clegg[5], Ben Pitcairn[5], Martin Weeks[5], Henning Kirk[6], and Erik Labahn[7]

[1]Department of Earth Sciences and Engineering, Imperial College London, UK

[2]Ocean and Earth Science, National Oceanography Centre Southampton, UK

[3]Department of Earth Sciences, Durham University, Durham, UK

[4]Department of Earth Ocean & Ecological Sciences, University of Liverpool, UK

[5]OBIF, UK

[6]DEPAS, Germany

[7]KUM, Germany

Acknowledgments
This work was funded under Natural Environment Research Council (NERC) Grants NE/K010743/1 and NE/K010654/1 (VoiLA). We thank the captain, John Leask, officers, crew, and science party members who sailed on RRS *James Cook* cruise JC149-leg3 (science party members are listed in Appendix A2) (Collier, 2017). We thank the UK Ocean-Bottom Instrumentation Facility (Minshull et al., 2005) and the German Instrument Pool for Amphibian Seismology (DEPAS), hosted by the Alfred Wegener Institute Bremerhaven, for providing the ocean-bottom seismometers. We thank the members of the VoiLA consortium for their contributions to this paper (for a full list of VoiLA consortium members, see Appendix A1). This article was greatly improved by feedback from Matthias Delescluse and two anonymous reviewers. Swath bathymetry and wide-angle seismic data from cruise JC149 are available from the Marine Geoscience Data System (http://www.marine-geo.org/tools/search/entry.php?id=JC149, DOI: 10.26022/IEDA/327347).

References

Abrams, L. J., Detrick, R. S., & Fox, P. J. (1988). Morphology and crustal structure of the Kane fracture zone transverse ridge. *Journal of Geophysical Research—Solid Earth*, *93*(B4), 3195–3210. https://doi.org/10.1029/JB093iB04p03195

Allen, R., Collier, J., Stewart, A., Henstock, T., Goes, S., Rietbrock, A., & Team, V. L. A. (2019). The role of arc migration in the development of the Lesser Antilles: A new tectonic model for the Cenozoic evolution of the eastern Caribbean. *Geology*, *47*(9), 891–895. https://doi.org/10.1130/G46708.1

Anonymous (1972). Penrose field conference on ophiolites. *Geotimes*, *17*(12), 24–25.

Bird, P. (2003). An updated digital model of plate boundaries. *Geochemistry, Geophysics, Geosystems*, *4*(3).

Blackman, D., B. Ildefonse, B. John, Y. Ohara, D. Miller, C. MacLeod, and Expedition Scientists (2006), Oceanic core complex formation, Atlantis Massif. Paper presented at Proc. Ocean Drill. Program Sci. Results.

Blackman, D. K., Abe, N., Carlson, R. L., Guerin, G., Ildefonse, B., & Kumpf, A. (2019). Seismic properties of gabbroic sections in oceanic core complexes: Constraints from seafloor drilling. *Marine Geophysical Research*, *40*(4), 557–569. https://doi.org/10.1007/s11001-019-09385-7

Blackman, D. K., Canales, J. P., & Harding, A. (2009). Geophysical signatures of oceanic core complexes. *Geophysical Journal International*, *178*(2), 593–613. https://doi.org/10.1111/j.1365-246X.2009.04184.x

Blackman, D. K., & Collins, J. A. (2010). Lower crustal variability and the crust/mantle transition at the Atlantis Massif oceanic core complex. *Geophysical Research Letters*, *37*(24), n/a. https://doi.org/10.1029/2010gl045165

Blackman, D. K., Slagle, A., Guerin, G., & Harding, A. (2014). Geophysical signatures of past and present hydration within a young oceanic core complex. *Geophysical Research Letters*, *41*(4), 1179–1186. https://doi.org/10.1002/2013GL058111

Canales, J. P. (2010). Small-scale structure of the Kane oceanic core complex, Mid-Atlantic Ridge 23°30′N, from waveform tomography of multichannel seismic data. *Geophysical Research Letters*, *37*(21), n/a. https://doi.org/10.1029/2010gl044412

Canales, J. P., Collins, J. A., Escartín, J., & Detrick, R. S. (2000). Seismic structure across the rift valley of the Mid-Atlantic Ridge at 23°20′ (MARK area): Implications for crustal accretion processes at slow spreading ridges. *Journal of Geophysical Research—Solid Earth*, *105*(B12), 28411–28425. https://doi.org/10.1029/2000JB900301

Canales, J. P., Detrick, R. S., Lin, J., Collins, J. A., & Toomey, D. R. (2000). Crustal and upper mantle seismic structure beneath the rift mountains and across a nontransform offset at the Mid-Atlantic Ridge (35°N). *Journal of Geophysical Research—Solid Earth*, *105*(B2), 2699–2719. https://doi.org/10.1029/1999JB900379

Canales, J. P., Dunn, R. A., Arai, R., & Sohn, R. A. (2017). Seismic imaging of magma sills beneath an ultramafic-hosted hydrothermal system. *Geology*, *45*(5), 451–454. https://doi.org/10.1130/G38795.1

Canales, J. P., Sohn, R. A., & Demartin, B. J. (2007). Crustal structure of the Trans-Atlantic Geotraverse (TAG) segment (Mid-Atlantic Ridge, 26°10′N): Implications for the nature of hydrothermal circulation and detachment faulting at slow spreading ridges. *Geochemistry, Geophysics, Geosystems*, *8*(8), n/a. https://doi.org/10.1029/2007GC001629

Canales, J. P., Tucholke, B. E., Xu, M., Collins, J. A., & DuBois, D. L. (2008). Seismic evidence for large-scale compositional heterogeneity of oceanic core complexes. *Geochemistry, Geophysics, Geosystems*, *9*(8), n/a. https://doi.org/10.1029/2008gc002009

Cann, J. R., Blackman, D. K., Smith, D. K., McAllister, E., Janssen, B., Mello, S., et al. (1997). Corrugated slip surfaces formed at ridge-transform intersections on the Mid-Atlantic Ridge. *Nature*, *385*(6614), 329–332. https://doi.org/10.1038/385329a0

Cann, J. R., Smith, D. K., Escartin, J., & Schouten, H. (2015). Tectonic evolution of 200 km of Mid-Atlantic Ridge over 10 million years: Interplay of volcanism and faulting. *Geochemistry, Geophysics, Geosystems*, *16*(7), 2303–2321. https://doi.org/10.1002/2015gc005797

Cannat, M. (1993). Emplacement of mantle rocks in the sea-floor at mid-ocean ridges. *Journal of Geophysical Research—Solid Earth*, *98*(B3), 4163–4172. https://doi.org/10.1029/92jb02221

Cannat, M., Lagabrielle, Y., Bougault, H., Casey, J., deCoutures, N., Dmitriev, L., & Fouquet, Y. (1997). Ultramafic and gabbroic exposures at the Mid-Atlantic Ridge: Geological mapping in the 15°N region. *Tectonophysics*, *279*(1–4), 193–213. https://doi.org/10.1016/S0040-1951(97)00113-3

Carbotte, S. M., Smith, D. K., Cannat, M., & Klein, E. M. (2016). Tectonic and magmatic segmentation of the Global Ocean Ridge System: A synthesis of observations. *Geological Society, London, Special Publications*, *420*(1), 249–295. https://doi.org/10.1144/sp420.5

Christeson, G., Goff, J., & Reece, R. (2019). Synthesis of oceanic crustal structure from two-dimensional seismic profiles. *Reviews of Geophysics*, *57*(2), 504–529. https://doi.org/10.1029/2019RG000641

Collier, J., Henstock, T., Peirce, C., & Watts, A. (1998). A detailed geophysical study in the Canary Basin (eastern Atlantic): Implications for the internal structure of 130 Ma oceanic crust. *Geophysical Journal International*, *135*(3), 943–963. https://doi.org/10.1046/j.1365-246X.1998.00675.x

Collier, J. S. (2017), VoiLA—Volatile recycling in the Lesser Antilles arc: RRS James Cook cruise report JC149, *Imperial College London*, https://www.bodc.ac.uk/resources/inventories/cruise_inventory/reports/jc149.pdf, 1–161.

Collins, J. A., Blackman, D. K., Harris, A., & Carlson, R. L. (2009). Seismic and drilling constraints on velocity structure and reflectivity near IODP Hole U1309D on the central dome of Atlantis Massif, Mid-Atlantic Ridge 30°N. *Geochemistry, Geophysics, Geosystems*, *10*(1), n/a. https://doi.org/10.1029/2008gc002121

Dannowski, A., Grevemeyer, I., Ranero, C. R., Ceuleneer, G., Maia, M., Morgan, J. P., & Gente, P. (2010). Seismic structure of an oceanic core complex at the Mid-Atlantic Ridge, 22°19′N. *Journal of Geophysical Research—Solid Earth*, *115*(B7), B07106. https://doi.org/10.1029/2009JB006943

Dannowski, A., Morgan, J. P., Grevemeyer, I., & Ranero, C. R. (2018). Enhanced mantle upwelling/melting caused segment propagation, oceanic core complex die off, and the death of a transform fault: The Mid-Atlantic Ridge at 21.5°. *N, Journal of Geophysical Research: Solid Earth*, *123*(2), 941–956.

Delescluse, M., Funck, T., Dehler, S. A., Louden, K. E., & Watremez, L. (2015). The oceanic crustal structure at the extinct, slow to ultraslow Labrador Sea spreading center. *Journal of Geophysical Research—Solid Earth*, *120*(7), 5249–5272. https://doi.org/10.1002/2014JB011739

de Martin, B. J., Sohn, R. A., Canales, J. P., & Humphris, S. E. (2007). Kinematics and geometry of active detachment faulting beneath the Trans-Atlantic Geotraverse (TAG) hydrothermal field on the Mid-Atlantic Ridge. *Geology*, *35*(8), 711–714. https://doi.org/10.1130/g23718a.1

Detrick, R., White, R., & Purdy, G. (1993). Crustal structure of North Atlantic fracture zones. *Reviews of Geophysics*, *31*(4), 439–458. https://doi.org/10.1029/93RG01952

Dick, H. J. B., Tivey, M. A., & Tucholke, B. E. (2008). Plutonic foundation of a slow-spreading ridge segment: Oceanic core complex at Kane Megamullion, 23°30′N, 45°20′W. *Geochemistry, Geophysics, Geosystems*, *9*(5), n/a. https://doi.org/10.1029/2007gc001645

Dunn, R. A., Arai, R., Eason, D. E., Canales, J. P., & Sohn, R. A. (2017). Three-dimensional seismic structure of the Mid-Atlantic Ridge: An investigation of tectonic, magmatic, and hydrothermal processes in the Rainbow area. *Journal of Geophysical Research—Solid Earth*, *122*(12), 9580–9602. https://doi.org/10.1002/2017JB015051

Dunn, R. A., Lekić, V., Detrick, R. S., & Toomey, D. R. (2005). Three-dimensional seismic structure of the Mid-Atlantic Ridge (35°N): Evidence for focused melt supply and lower crustal dike injection. *Journal of Geophysical Research—Solid Earth*, *110*(B9). https://doi.org/10.1029/2004JB003473

Escartín, J., & Canales, J. P. (2011). Detachments in oceanic lithosphere: Deformation, magmatism, fluid flow, and ecosystems. *Eos, Transactions American Geophysical Union*, *92*(4), 31–31. https://doi.org/10.1029/2011EO040003

Escartín, J., Mével, C., MacLeod, C. J., & McCaig, A. M. (2003). Constraints on deformation conditions and the origin of oceanic detachments: The Mid-Atlantic Ridge core complex at 15°45′N. *Geochemistry, Geophysics, Geosystems*, *4*(8). https://doi.org/10.1029/2002gc000472

Escartin, J., Smith, D. K., Cann, J., Schouten, H., Langmuir, C. H., & Escrig, S. (2008). Central role of detachment faults in accretion of slow-spreading oceanic lithosphere. *Nature*, *455*(7214), 790–794. https://doi.org/10.1038/nature07333

Grevemeyer, I., Hayman, N. W., Peirce, C., Schwardt, M., Van Avendonk, H. J., Dannowski, A., & Papenberg, C. (2018). Episodic magmatism and serpentinized mantle exhumation at an ultraslow-spreading centre. *Nature Geoscience*, *11*(6), 444–448. https://doi.org/10.1038/s41561-018-0124-6

Grevemeyer, I., Ranero, C. R., & Ivandic, M. (2018). Structure of oceanic crust and serpentinization at subduction trenches. *Geosphere*, *14*(2), 395–418. https://doi.org/10.1130/GES01537.1

Grevemeyer, I., & Weigel, W. (1997). Increase of seismic velocities in upper oceanic crust: The "superfast" Spreading East Pacific Rise at 14°14′S. *Geophysical Research Letters*, *24*(3), 217–220. https://doi.org/10.1029/96GL04005

Harding, J. L., Van Avendonk, H. J., Hayman, N. W., Grevemeyer, I., Peirce, C., & Dannowski, A. (2017). Magmatic-tectonic conditions for hydrothermal venting on an ultraslow-spread oceanic core complex. *Geology*, *45*(9), 839–842. https://doi.org/10.1130/G39045.1

Harmon, N., Rychert, C., Collier, J., Henstock, T., van Hunen, J., & Wilkinson, J. J. (2019). Mapping geologic features onto subducted slabs. *Geophysical Journal International*, *219*(2), 725–733. https://doi.org/10.1093/gji/ggz290

Henig, A. S., Blackman, D. K., Harding, A. J., Canales, J. P., & Kent, G. M. (2012). Downward continued multichannel seismic refraction analysis of Atlantis Massif oceanic core complex, 30°N, Mid-Atlantic Ridge. *Geochemistry, Geophysics, Geosystems*, *13*, Q0AG07. https://doi.org/10.1029/2012gc004059

Henstock, T. J., White, R. S., & McBride, J. H. (1996). Along-axis variability in crustal accretion at the Mid-Atlantic Ridge: Results from the OCEAN study. *Journal of Geophysical Research—Solid Earth*, *101*(B6), 13673–13688. https://doi.org/10.1029/96JB00092

Hooft, E., Detrick, R., Toomey, D., Collins, J., & Lin, J. (2000). Crustal thickness and structure along three contrasting spreading segments of the Mid-Atlantic Ridge, 33.5–35°. *N, Journal of Geophysical Research: Solid Earth*, *105*(B4), 8205–8226. https://doi.org/10.1029/1999JB900442

Hosford, A., Lin, J., & Detrick, R. S. (2001). Crustal evolution over the last 2 m.y. at the Mid-Atlantic Ridge OH-1 segment, 35°N. *Journal of Geophysical Research—Solid Earth*, *106*(B7), 13269–13285. https://doi.org/10.1029/2001jb000235

Houtz, R., & Ewing, J. (1976). Upper crustal structure as a function of plate age. *Journal of Geophysical Research*, *81*(14), 2490–2498. https://doi.org/10.1029/JB081i014p02490

Ildefonse, B., Blackman, D. K., John, B. E., Ohara, Y., Miller, D. J., & MacLeod, C. J. (2007). Oceanic core complexes and crustal accretion at slow-spreading ridges. *Geology*, *35*(7), 623. https://doi.org/10.1130/g23531a.1

Klitgord, K. D., & Schouten, H. (1986). Plate kinematics of the central Atlantic. In P. R. Vogt & B. E. Tucholke (Eds.), *The geology of North America* (pp. 351–378). Boulder, CO: Geological Society of America.

Korenaga, J., Holbrook, W., Kent, G., Kelemen, P., Detrick, R., Larsen, H. C., et al. (2000). Crustal structure of the southeast Greenland margin from joint refraction and reflection seismic tomography. *Journal of Geophysical Research—Solid Earth*, *105*(B9), 21591–21614. https://doi.org/10.1029/2000JB900188

Langmuir, C. H., Bender, J. F., & Batiza, R. (1986). Petrological and tectonic segmentation of the East Pacific Rise, 5°30′–14°30′N. *Nature*, *322*(6078), 422–429. https://doi.org/10.1038/322422a0

Larkin, S. P., & Levander, A. (1996). Wave-equation datuming for improving deep crustal seismic images. *Tectonophysics*, *264*(1–4), 371–379. https://doi.org/10.1016/S0040-1951(96)00137-0

Lin, J., & Phipps Morgan, J. (1992). The spreading rate dependence of three-dimensional mid-ocean ridge gravity structure. *Geophysical Research Letters*, *19*(1), 13–16. https://doi.org/10.1029/91GL03041

Lizarralde, D., Gaherty, J. B., Collins, J. A., Hirth, G., & Kim, S. D. (2004). Spreading-rate dependence of melt extraction at mid-ocean ridges from mantle seismic refraction data. *Nature*, *432*(7018), 744–747. https://doi.org/10.1038/nature03140

Ludwig, W. J., & Rabinowitz, P. D. (1980). Structure of Vema fracture zone. *Marine Geology*, *35*(1–3), 99–110. https://doi.org/10.1016/0025-3227(80)90024-9

Macdonald, K. C., Fox, P., Perram, L., Eisen, M., Haymon, R., Miller, S., et al. (1988). A new view of the mid-ocean ridge from the behaviour of ridge-axis discontinuities. *Nature*, *335*(6187), 217–225. https://doi.org/10.1038/335217a0

MacLeod, C., R. Searle, B. Murton, J. Casey, C. Mallows, S. Unsworth, et al. (2009), Life cycle of oceanic core complexes, *Earth and Planetary Science Letters*, *287*(3–4), 333–3-4, 344, DOI: https://doi.org/10.1016/j.epsl.2009.08.016.

MacLeod, C. J., Escartín, J., Banerji, D., Banks, G. J., Gleeson, M., Irving, D. H. B., et al. (2002). Direct geological evidence for oceanic detachment faulting: The Mid-Atlantic Ridge, 15°45′N. *Geology*, *30*(10), 879–882. https://doi.org/10.1130/0091-7613(2002)030%3C0879:Dgefod%3E2.0.Co;2

Minshull, T., Bruguier, N., & Brozena, J. (2003). Seismic structure of the Mid-Atlantic Ridge, 8–9°S. *Journal of Geophysical Research—Solid Earth*, *108*(B11), 2513. https://doi.org/10.1029/2002JB002360

Minshull, T., Sinha, M., & Peirce, C. (2005). Multi-disciplinary, sub-seabed geophysical imaging. *Sea Technology*, *46*(10), 27–31.

Minshull, T., White, R., Mutter, J., Buhl, P., Detrick, R., Williams, C., & Morris, E. (1991). Crustal structure at the Blake Spur fracture zone from expanding spread profiles. *Journal of Geophysical Research—Solid Earth*, *96*(B6), 9955–9984. https://doi.org/10.1029/91JB00431

Minshull, T. A., Muller, M. R., Robinson, C. J., White, R. S., & Bickle, M. J. (1998). Is the oceanic Moho a serpentinization front? In R. A. Mills, & K. Harrison (Eds.), *Modern ocean floor processes and the geological record*, (pp. 71–80). London: Geological Society.

Mithal, R., & Mutter, J. C. (1989). A low-velocity zone within the layer 3 region of 118 Myr old oceanic crust in the western North Atlantic. *Geophysical Journal International*, *97*(2), 275–294. https://doi.org/10.1111/j.1365-246X.1989.tb00501.x

Müller, R. D., & Roest, W. R. (1992). Fracture zones in the North Atlantic from combined Geosat and Seasat data. *Journal of Geophysical Research—Solid Earth*, *97*(B3), 3337–3350. https://doi.org/10.1029/91jb02605

Müller, R. D., Royer, J.-Y., Cande, S. C., Roest, W. R., & Maschenkov, S. (1999). New constraints on the Late Cretaceous/Tertiary plate tectonic evolution of the Caribbean. In P. Mann (Ed.), *Sedimentary basins of the world* (pp. 33–59). Amsterdam: Elsevier Science, B.V.

Müller, R. D., & Smith, W. H. (1993). Deformation of the oceanic crust between the North American and South American plates. *Journal of Geophysical Research—Solid Earth*, *98*(B5), 8275–8291. https://doi.org/10.1029/92jb02863

Müller, R. D., Zahirovic, S., Williams, S. E., Cannon, J., Seton, M., Bower, D. J., et al. (2019). A global plate model including lithospheric deformation along major rifts and orogens since the Triassic. *Tectonics*, *38*(6), 1884–1907. https://doi.org/10.1029/2018TC005462

NAT Study Group (1985). North Atlantic Transect: A wide-aperture, two-ship multichannel seismic investigation of the oceanic crust. *Journal of Geophysical Research*, *90*(B12), 10321–10341. https://doi.org/10.1029/JB090iB12p10321

Ohara, Y., Okino, K., & Kasahara, J. (2007). Seismic study on oceanic core complexes in the Parece Vela back-arc basin. *Island Arc*, *16*(3), 348–360. https://doi.org/10.1111/j.1440-1738.2007.00591.x

Ohara, Y., Yoshida, T., Kato, Y., & Kasuga, S. (2001). Giant megamullion in the Parece Vela backarc basin. *Marine Geophysical Researches*, *22*(1), 47–61. https://doi.org/10.1023/A:1004818225642

Olive, J.-A., Behn, M. D., & Tucholke, B. E. (2010). The structure of oceanic core complexes controlled by the depth distribution of magma emplacement. *Nature Geoscience*, *3*(7), 491–495. https://doi.org/10.1038/ngeo888

Parnell-Turner, R., Sohn, R. A., Peirce, C., Reston, T. J., MacLeod, C. J., Searle, R. C., & Simão, N. M. (2017). Oceanic detachment faults generate compression in extension. *Geology*, *45*(10), 923–926. https://doi.org/10.1130/G39232.1

Paulatto, M., Canales, J. P., Dunn, R. A., & Sohn, R. A. (2015). Heterogeneous and asymmetric crustal accretion: New constraints from multibeam bathymetry and potential field data from the Rainbow area of the Mid-Atlantic Ridge (36°15′N). *Geochemistry, Geophysics, Geosystems*, *16*(9), 2994–3014. https://doi.org/10.1002/2015GC005743

Peirce, C., Reveley, G., Robinson, A., Funnell, M., Searle, R., Simão, N., et al. (2019). Constraints on crustal structure of adjacent OCCs and segment boundaries at 13°N on the Mid-Atlantic Ridge. *Geophysical Journal International*, *217*(2), 988–1010. https://doi.org/10.1093/gji/ggz074

Phipps Morgan, J., & Chen, Y. J. (1993). The genesis of oceanic crust: Magma injection, hydrothermal circulation, and crustal flow. *Journal of Geophysical Research—Solid Earth*, *98*(B4), 6283–6297. https://doi.org/10.1029/92JB02650

Planert, L., Flueh, E. R., & Reston, T. J. (2009). Along-and across-axis variations in crustal thickness and structure at the Mid-Atlantic Ridge at 5°S obtained from wide-angle seismic tomography: Implications for ridge segmentation. *Journal of Geophysical Research—Solid Earth*, *114*(B9), B09102. https://doi.org/10.1029/2008JB006103

Potts, C., Calvert, A., & White, R. (1986). Crustal structure of Atlantic Fracture zones—III. The Tydeman fracture zone. *Geophysical Journal of the Royal Astronomical Society*, *86*(3), 909–942. https://doi.org/10.1111/j.1365-246X.1986.tb00668.x

Potts, C., White, R., & Louden, K. (1986). Crustal structure of Atlantic fracture zones—II. *The Vema fracture zone and transverse ridge, Geophysical Journal International*, *86*(2), 491–513.

Reston, T. J., and C. R. Ranero (2011), The 3-D geometry of detachment faulting at mid-ocean ridges, *Geochemistry, Geophysics, Geosystems*, *12*(7), n/a-n/a, https://doi.org/10.1029/2011gc003666

Reston, T. J., Ranero, C. R., Ruoff, O., Perez-Gussinye, M., & Danobeitia, J. J. (2004). Geometry of extensional faults developed at slow-spreading centres from pre-stack depth migration of seismic reflection data in the Central Atlantic (Canary Basin). *Geophysical Journal International*, *159*(2), 591–606. https://doi.org/10.1111/j.1365-246X.2004.02444.x

Sandwell, D. T., Müller, R. D., Smith, W. H., Garcia, E., & Francis, R. (2014). New global marine gravity model from CryoSat-2 and Jason-1 reveals buried tectonic structure. *Science*, *346*(6205), 65–67. https://doi.org/10.1126/science.1258213

Seher, T., Crawford, W. C., Singh, S. C., Cannat, M., Combier, V., & Dusunur, D. (2010). Crustal velocity structure of the Lucky Strike segment of the Mid-Atlantic Ridge at 37°N from seismic refraction measurements. *Journal of Geophysical Research—Solid Earth*, *115*(B3). https://doi.org/10.1029/2009jb006650

Smith, D. K., Cann, J. R., & Escartín, J. (2006). Widespread active detachment faulting and core complex formation near 13°N on the Mid-Atlantic Ridge. *Nature*, *442*(7101), 440–443. https://doi.org/10.1038/nature04950

Smith, D. K., Escartin, J., Cannat, M., Tolstoy, M., Fox, C. G., Bohnenstiehl, D. R., & Bazin, S. (2003). Spatial and temporal distribution of seismicity along the northern Mid-Atlantic Ridge (15°–35°N). *Journal of Geophysical Research—Solid Earth*, *108*(B3). https://doi.org/10.1029/2002jb001964

Smith, D. K., Escartín, J., Schouten, H., & Cann, J. R. (2008). Fault rotation and core complex formation: Significant processes in seafloor formation at slow-spreading mid-ocean ridges (Mid-Atlantic Ridge, 13°–15°N). *Geochemistry, Geophysics, Geosystems*, *9*(3), n/a. https://doi.org/10.1029/2007gc001699

Spathopoulos, F., & Jones, E. (1993). Seismic evidence for anomalous crustal structure beneath Mesozoic fracture zones in the Gambia Basin, eastern equatorial Atlantic. *Tectonophysics*, *225*(3), 205–217. https://doi.org/10.1016/0040-1951(93)90280-W

Tolstoy, M., Harding, A. J., & Orcutt, J. A. (1993). Crustal thickness on the Mid-Atlantic Ridge: Bull's-eye gravity anomalies and focused accretion. *Science*, *262*(5134), 726–729. https://doi.org/10.1126/science.262.5134.726

Tucholke, B. E., Behn, M. D., Buck, W. R., & Lin, J. (2008). Role of melt supply in oceanic detachment faulting and formation of mega-mullions. *Geology*, *36*(6), 455–458. https://doi.org/10.1130/G24639A.1

Tucholke, B. E., Lin, J., & Kleinrock, M. C. (1998). Megamullions and mullion structure defining oceanic metamorphic core complexes on the Mid-Atlantic Ridge. *Journal of Geophysical Research—Solid Earth*, *103*(B5), 9857–9866. https://doi.org/10.1029/98JB00167

Wessel, P., Matthews, K. J., Müller, R. D., Mazzoni, A., Whittaker, J. M., Myhill, R., & Chandler, M. T. (2015). Semiautomatic fracture zone tracking. *Geochemistry, Geophysics, Geosystems*, *16*(7), 2462–2472.

White, R. S., McKenzie, D., & O'Nions, R. K. (1992). Oceanic crustal thickness from seismic measurements and rare earth element inversions. *Journal of Geophysical Research—Solid Earth*, *97*(B13), 19683–19715. https://doi.org/10.1029/92JB01749

Whitmarsh, R., Keen, C., Steinmetz, L., Tomblin, J., Whitmarsh, R., Donegan, M., et al. (1983). A lithospheric seismic refraction profile in the western North Atlantic Ocean. *Geophysical Journal of the Royal Astronomical Society*, *75*(1), 23–69.

Wolfe, C. J., Purdy, G., Toomey, D. R., & Solomon, S. C. (1995). Microearthquake characteristics and crustal velocity structure at 29°N on the Mid-Atlantic Ridge: The architecture of a slow spreading segment. *Journal of Geophysical Research—Solid Earth*, *100*(B12), 24449–24472. https://doi.org/10.1029/95JB02399

Xu, M., Canales, J. P., Tucholke, B. E., & DuBois, D. L. (2009). Heterogeneous seismic velocity structure of the upper lithosphere at Kane oceanic core complex, Mid-Atlantic Ridge. *Geochemistry, Geophysics, Geosystems*, *10*(10), n/a. https://doi.org/10.1029/2009gc002586

Zelt, C., & Smith, R. (1992). Seismic traveltime inversion for 2-D crustal velocity structure. *Geophysical Journal International*, *108*(1), 16–34. https://doi.org/10.1111/j.1365-246X.1992.tb00836.x

Zelt, C. A., & Barton, P. J. (1998). Three-dimensional seismic refraction tomography: A comparison of two methods applied to data from the Faeroe Basin. *Journal of Geophysical Research—Solid Earth*, *103*(B4), 7187–7210. https://doi.org/10.1029/97JB03536

Zhao, M. H., Canales, J. P., & Sohn, R. A. (2012). Three-dimensional seismic structure of a Mid-Atlantic Ridge segment characterized by active detachment faulting (Trans-Atlantic Geotraverse, 25°55′N–26°20′N). *Geochemistry, Geophysics, Geosystems*, *13*(11), 2012GC004454. https://doi.org/10.1029/2012gc004454